AD-A087 699 RICE UNIV HOUSTON TX F/G 4/1
QUANTITATIVE SIMULATION OF A MAGNETOSPHERIC SUBSTORM. 1. MODEL --ETC(U)
JAN 80 M HAREL, R A WOLF, R W SPIRO F19628-77-C-0005
UNCLASSIFIED SCIENTIFIC-2 AFGL-TR-80-0128 NL

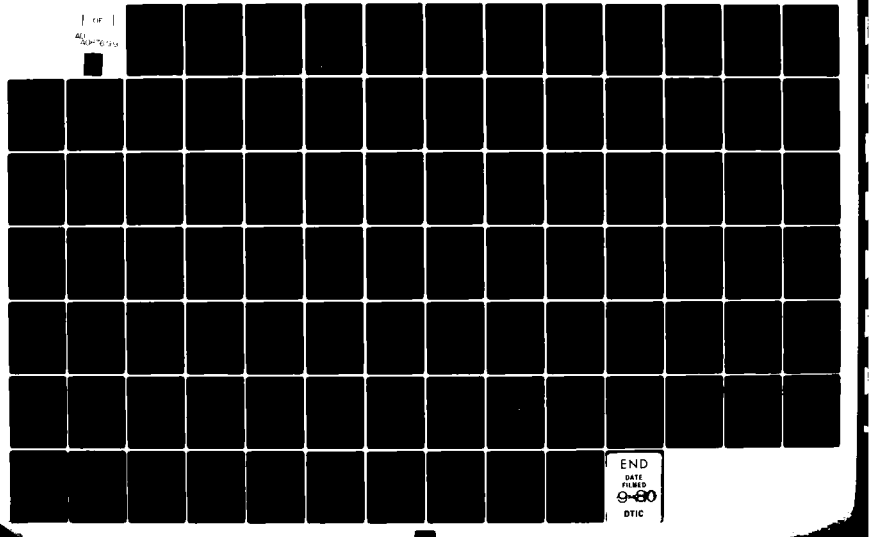

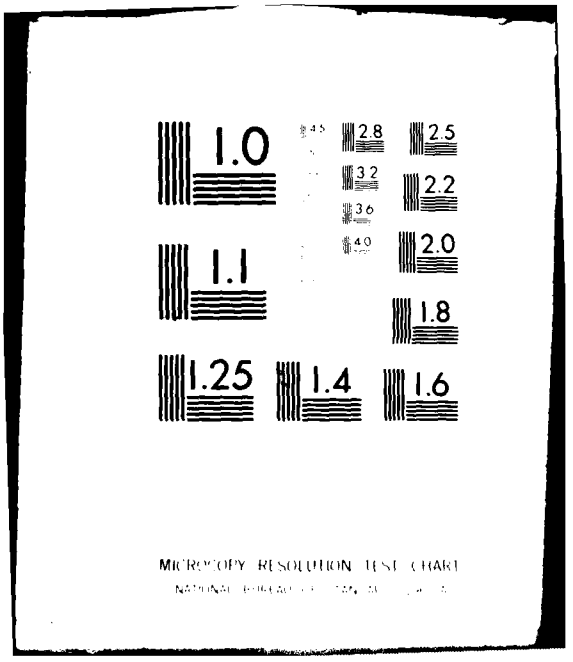
1.0
2.8
2.5
3.2
2.2
3.6
4.0
2.0
1.1
1.8
1.25
1.4
1.6
MICROCOPY RESOLUTION TEST CHART

LEVEL II

AFGL-TR-80-0128

QUANTITATIVE SIMULATION OF A MAGNETOSPHERIC SUBSTORM
1. Model Logic and Overview

M. Harel
R. A. Wolf
R. W. Spiro
P. H. Reiff
C. -K. Chen
W. J. Burke
F. J. Rich
M. Smiddy

William Marsh Rice University
6100 South Main Street
Houston, Texas 77005

Scientific Report No. 2

23 January 1980

AIR FORCE GEOPHYSICS LABORATORY
AIR FORCE SYSTEMS COMMAND
UNITED STATES AIR FORCE
HANSCOM AFB, MASSACHUSETTS 01731

Unclassified

SECURITY CLASSIFICATION OF THIS PAGE (When Data Entered)

18 19 REPORT DOCUMENTATION PAGE

READ INSTRUCTIONS BEFORE COMPLETING FORM

1. REPORT NUMBER: AFGL-TR-80-0128
2. GOVT ACCESSION NO.: AD-A087699
3. RECIPIENT'S CATALOG NUMBER:

4. TITLE (and Subtitle): 6 Quantitative Simulation of a Magnetospheric Substorm, 1. Model Logic and Overview
5. TYPE OF REPORT & PERIOD COVERED: 14 Scientific -2 Report No. 2
6. PERFORMING ORG. REPORT NUMBER:

7. AUTHOR(s): 10 M. Harel R. A. Wolf R. W. Sprio P. H. Reiff C.-K. Chen ~~W. J. Burke, F. J. Rich~~ and M. Smiddy
8. CONTRACT OR GRANT NUMBER(s): 15 F19628-77-C-0005

9. PERFORMING ORGANIZATION NAME AND ADDRESS: William Marsh Rice University, 6100 South Main Street, Houston, Texas 77005 (408198)
10. PROGRAM ELEMENT, PROJECT, TASK AREA & WORK UNIT NUMBERS: 61102F, 2311G1AH 16 17 G-1

11. CONTROLLING OFFICE NAME AND ADDRESS: U.S. Air Force Geophysics Laboratory, Hanscom AFB, Massachusetts 01731, Contract Monitor; Capt. David Hardy (PHG)
12. REPORT DATE: 11 23 Jan~~uary~~ 1980
13. NUMBER OF PAGES: 91

14. MONITORING AGENCY NAME & ADDRESS (if different from Controlling Office): 12 72
15. SECURITY CLASS. (of this report): Unclassified
15a. DECLASSIFICATION DOWNGRADING SCHEDULE:

16. DISTRIBUTION STATEMENT (of this Report)

Approved for public release; distribution unlimited.

17. DISTRIBUTION STATEMENT (of the abstract entered in Block 20, if different from Report)

18. SUPPLEMENTARY NOTES

19. KEY WORDS (Continue on reverse side if necessary and identify by block number)

Magnetosphere
Ionosphere
Substorm
Ring Current
Electric Fields

20. ABSTRACT (Continue on reverse side if necessary and identify by block number)

Abstract

This and the following two papers report results of the first comprehensive computer simulation of the behavior of the earth's inner magnetosphere during a substorm-type event.

(Please see other side)

DD FORM 1 JAN 73 1473 EDITION OF 1 NOV 65 IS OBSOLETE

Unclassified

305 750

We have developed a self-consistent quantitative model to compute electric fields, currents and the resulting plasma flow in the inner-magnetosphere/ionosphere system ($L \leq 10$); parallel electric fields and ionospheric neutral winds are not included. The model was tested for a substorm-type event that occurred on September 19, 1976. Satellite data (primarily from the Air Force S3-2 satellite) were used extensively both for boundary conditions and for comparisons with model predictions. Other data were also used as input for our time-dependent magnetic field and conductivity models.

The S3-2 data for the event show some novel features, independent of the simulation. Dawn-dusk electric fields show a general correlation with the east-west magnetic field perturbations. Unexpectedly, two of the passes display substantial regions of sunward plasma flow poleward of the main part of the region-1 Birkeland currents.

The cross-polar-cap potential drops computed from the data represent the first effort at satellite monitoring of this important parameter during various phases of a substorm, and show an important enhancement during the substorm.

Numerical results from these first-try simulations were consistent with most of the established features of convection in the inner magnetosphere, such as generally sunward flow, shielding of the potential electric field for $L \leq 5$ and the tendency for stronger electric fields on the dusk side than on the dawn side. In addition, the model reproduces some typical substorm phenomena, such as energy-dependent particle injection with a dawn-dusk asymmetry and establishment of a partial ring current.

This paper deals with model logic, methodology, inputs and overview of results; the succeeding two papers give detailed analyses and comparisons with data.

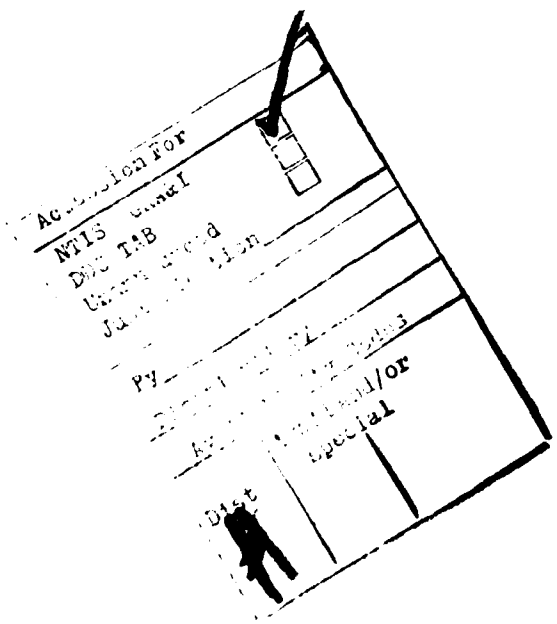

I. INTRODUCTION

The present three papers are the latest reports on a longstanding effort at a quantitative model of plasma flow, particle distributions and electric currents in the inner magnetosphere and ionosphere, and at theoretically modeling the time dependent physical processes that take place.

In the past few years our group has developed a program for self-consistent computer simulation of the magnetosphere-ionosphere system [Wolf, 1970; Jaggi and Wolf, 1973; Wolf, 1974; Harel and Wolf, 1976]. In those papers the emphasis was put on "steady state simulation", where our model was tested for "average" magnetospheric conditions. Over this period, our work progressed to include more and more physical processes while the mechanics of our computer simulation were improved. Although some interesting and meaningful insights into the magnetosphere were obtained from such quiet-time simulations, the magnetosphere is seldom, if ever, close to a steady state, and the most exciting phenomena occur during disturbed times. We have therefore proceeded to simulate a substorm-type event and to compare our theoretical results with satellite data.

The concept of magnetospheric convection was first formulated in the early 1960's [Axford and Hines, 1961; Dungey, 1961; and Cole, 1961]. Some sort of effective friction between the solar wind and the magnetosphere was seen to cause this plasma circulation, resulting in antisunward flow in the outer magnetosphere, and sunward flow in the inner regions. (See reviews by Axford [1969] and Stern [1977]). The

role of ionospheric conductivity and Birkeland currents in regulating this sunward convection was partly understood in the mid-sixties [Karlson, 1963; Fejer, 1964; Block, 1966]. However, the interactions are many and complex, and many of the subsequent studies modeled only a portion of the system. One group of models concentrated primarily on the ionosphere [Volland, 1975; Heppner, 1977; Yasuhara and Akasofu, 1977; Nisbet et al., 1978; Nopper and Carovillano, 1978, 1979; Kamide and Matsushita, 1979a and b; Gizler et al., 1979]. Another group attempted modeling the ring current injection using assumed semiempirical electric fields [e.g., McIlwain, 1974; Roederer and Hones, 1974; Konradi et al., 1976; Cowley, 1976; Kivelson, 1976; Ejiri et al., 1977, 1978; Smith et al., 1979]. Such models, though useful, were generally limited in scope. The more comprehensive efforts at quantitative modeling of the complete magnetosphere-ionosphere system were obviously more complex [Wolf, 1970; Swift, 1971; Vasyliunas, 1970, 1972; Jaggi and Wolf, 1973; Mal'tsev, 1974; Wolf, 1974; Harel and Wolf, 1976].

The complexity of the system, its nonlinearity and its strong time-dependence (especially during disturbed times) make quantitative modeling difficult. We have developed an approach of coupling the available time-dependent input data with the solution of the differential equations governing the large scale motions of plasmas in the magnetosphere-ionosphere system. While some of the data are used as input, other data are used for testing our model predictions. We have chosen to model the substorm-type event of September 19, 1976 whose onset occurred at roughly 1000 UT. Given input data (mostly from the S3-2 satellite) our program computed, self-consistently, the time evolution of

electric fields, plasma flow velocities, electric currents and ring current injection. Of course, the fact that the critical spacecraft observations cannot be made continuously in universal time, at all L-values and local times in the magnetosphere, means that our model input data, based mainly on interpolations of available observations, contain far less spatial and temporal structure than was actually present on 19 September 1976.

It should be emphasized that in this paper as well as in the two following papers we have not "fudged" our input assumptions to improve agreement between theoretical predictions and observations. We consider this to be a "true first run" simulation. Analysis of these initial results will enable us to improve our initial and boundary conditions to yield better agreement with data in future simulations. We will refer to the following two papers, Harel et al. [1980] and Spiro et al. [1980] as Papers 2 and 3, respectively.

While the present first-run simulations are an imprecise representation of what actually happened in the magnetosphere and ionosphere on 19 September 1976, they provide many important insights into the behavior of the inner magnetosphere during substorms and other periods of strong convection.

II. FORMULATION AND LOGIC

Our model concentrates on the inner magnetosphere, specifically the region where magnetic field lines are certainly closed. We feel that the complexity of the outer magnetospheric dynamics does not lend itself to detailed quantitative modeling yet. Therefore, we apply our boundary conditions just inside of the magnetopause boundary layer, which roughly maps to the polar-cap boundary, and attempt a self-consistent solution equatorward of that region (Fig. 1).

A. Conservation equations

The coupling between the magnetosphere and the ionosphere requires simultaneous solution of the current- and particle-conservation equations in both regions. Drifts of plasma-sheet and ring-current particles are computed under the assumption that the pitch angles of the particles are scattered many times in the time it takes them to drift a significant distance in the magnetosphere [Vasyliunas, 1968; Kennel 1969]. Within this isotropic-pitch-angle approximation, it is convenient to define a parameter λ, which is related to the thermal kinetic energy, E, by

$$E = \lambda(\int ds/B)^{-2/3} \qquad (1)$$

where $\int ds/B$ = volume of a magnetic flux tube with unit magnetic flux. It is shown in the Appendix that this "energy invariant", λ, and also the "number invariant", $\eta(\lambda)$, which is the number of particles per unit magnetic flux with energy invariant λ, are constant along the drift path of a particle.

We characterize the plasma-sheet particle population in terms of 21 species, such that each particle of species k has charge q_k and energy

invariant λ_k. Ten species are ions, ten are electrons and one is cold plasma; electron precipitation is taken into account approximately by considering two species for each λ-value, corresponding to different amounts of loss, as discussed in section V. For simplicity, we assume a uniform, steady particle source in the tail so that $\eta_k(\underset{\sim}{x})$ is equal to a constant value η_k. (Earthward of the inner edge for species s, $\eta_k(\underset{\sim}{x})$ is, of course, zero).

The drift velocity of the equatorial crossing point of a particle of species k is given by

$$\underset{\sim}{v}_k = B_e^{-1} \hat{z} \times (\nabla_e V_{eff} - \underset{\sim}{E}_{ind}) \tag{2}$$

where

$$V_{eff} = V + V_{cor} + (\lambda_k/q_k)(\int ds/B)^{-2/3} \tag{3}$$

B_e = equatorial magnetic field, $\hat{z}$ = unit vector normal to the equatorial plane (northward); ∇_e = gradient operator in the equatorial plane, V = electrostatic potential in a reference frame that rotates with the earth, V_{cor} = corotation potential [equation 3 of Jaggi and Wolf, 1973], $\underset{\sim}{E}_{ind}$ = induction electric field.

We have chosen $\underset{\sim}{E}_{ind}$ such that

$$\underset{\sim}{v}_{ecp}(\underset{\sim}{x}_e,t) = (\underset{\sim}{E}_{ind}(\underset{\sim}{x}_e,t) \times \underset{\sim}{B}_e)/B_e^2 \tag{4}$$

when $\underset{\sim}{v}_{ecp}(\underset{\sim}{x}_e,t)$ is the velocity of the equatorial crossing point of a magnetic field line whose equatorial crossing point is $\underset{\sim}{x}_e$ at time t and whose ionospheric crossing point is constant in time.

The third term in equation 3, which represents gradient and curvature drift, is derived in the Appendix. We use equation 2 to follow the motion of the inner edge of each particle species k (see section V.C).

The gradient/curvature drift current, mapped along field lines to the equatorial plane, is given by

$$\underset{\sim}{j}_e(\underset{\sim}{x}_e) = \sum_k \lambda_k \eta_k \, \hat{z} \times \nabla_e \left[\left(\int ds/B \right)^{-2/3} \right] \tag{5}$$

where $\underset{\sim}{j}_e$ = current per unit length in the equatorial plane, and the sum includes the species k that are present at $\underset{\sim}{x}_e$. Conservation of current in the magnetosphere then gives

$$j_{\|e} = -\nabla_e \cdot \underset{\sim}{j}_e = -\nabla_e \left(\sum_k \lambda_k \eta_k \right) \cdot \left\{ \hat{z} \times \nabla_e \left[\left(\int ds/B \right)^{-2/3} \right] \right\} \tag{6}$$

where $j_{\|e}$ = Birkeland current per unit area away from the equatorial plane. Magnetization current has been ignored becuase it has no divergence. Note that (6) implies that Birkeland currents are generated only near the inner edge of the plasma sheet, where there are gradients in the η_k's.

We now equate the current out of the equatorial plane to the total current into the ionosphere (both hemispheres). Assuming that the induction electric field is very small compared to the potential electric field in the ionosphere, neglecting vertical electric field in the conducting region of the ionosphere, and neglecting $\underset{\sim}{v}_n \times \underset{\sim}{B}$, where $\underset{\sim}{v}_n$ = neutral-wind velocity, we can derive a simplified form of the ionospheric-current conservation equation:

$$\nabla_h \cdot [\underset{\approx}{\Sigma} \cdot (-\nabla_h V)] = j_{\parallel i} \qquad (7)$$

where ∇_h represents a horizontal gradient operator in the ionosphere, $\underset{\approx}{\Sigma}$ = height-integrated ionospheric conductivity (both hemispheres), and $j_{\parallel i}$, the current per unit area down into the ionosphere, is given by

$$j_{\parallel i} = (|B_{ir}|/B_e) j_{\parallel e} \qquad (8)$$

where B_{ir} = radial component of the magnetic field at the ionosphere. By using the same V in (3) and (7) we implicitly assume $\underset{\sim}{E} \cdot \underset{\sim}{B} = 0$.

B. Logical loop

Table 1 summarizes the assumptions of our model; model logic is illustrated in Figure 2. The basic logical loop (the central pentagon of the figure) is a modification of a diagram given by Vasyliunas [1970]. Dashed lines mark future additions to our program which are not included in the present simulation. Starting at a given time T with a given hot-particle distribution in the magnetosphere (section IV.D), estimated from average plasma-sheet particle data in the present case (upper box), we proceed counter-clockwise. We first solve equation 6 for the divergence of the gradient/curvature drift current in the magnetosphere. An important input for this calculation is the magnetic field model. Ideally, we would like to have a self-consistent, time-dependent magnetic field model (an attempt to develop such a model based on pressure balance between field and particle pressure developed numerical noise and was postponed). For the present simulation we have used a superposition of the Olson-Pfitzer [1974] analytic model and a time-dependent "substorm current loop" that simulates the effects of an induction electric field. The details of this loop will be discussed in

section IV.B.

Knowing the divergence of current in the equatorial plane, we solve equations 6 and 8 for the field-aligned currents into the ionosphere, and equate them to the divergence of the ionospheric current using (7). A semi-empirical height-integrated ionospheric conductivity model has been developed, details of which are presented in section IV.C. Equation 7 is an elliptic equation in two dimensions that can be solved numerically for the potential V, given the conductivity tensor and $j_{\parallel i}$. Our boundary conditions are the following:

(i) Zero electric current across the equator (this condition follows from the assumed symmetry between the hemispheres, a reasonable assumption for 19 September, which is near equinox; actually the condition we apply is that of zero current across latitude 21°).

(ii) Specified potential V on the polar boundary. Hereafter (including papers 2 and 3) we use the term "polar boundary" to denote the equatorward boundary of the region-1 Birkeland current, which should be distinguished from "polar cap boundary" that is commonly defined by electric field reversals (see further discussion in Section IV.A). Because of the irregularities of the polar boundary we actually specified the potential on a circle that encompasses the polar boundary. The distribution of the potential around this curve has the general form suggested by Figure 1 of Heelis et al.[1976]; the magnitude of the potential drop was estimated from real-time observations (see section IV. A).

Given the ionospheric potential distribution we use the magnetic-field model to map V to the equatorial plane. In the present

simulation we neglect the component of $\underset{\sim}{E}$ that is parallel to $\underset{\sim}{B}$, although we believe that a few kV potential drop over limited regions would not affect our results substantially. We proceed with the logic loop to calculate magnetospheric electric fields. The total electric field is the sum of the potential electric field and the induction field calculated by means of letting the equatorial crossing point of the field line vary in time. This motion corresponds to $\underset{\sim}{E} \times \underset{\sim}{B}$ drift in an induction electric field. We should mention that this is only one of several ways to introduce the induction electric field; this one was chosen for its simplicity (see equation 4 in II.A).

Given the potential electric field, the motion of equatorial crossing points due to induction, and the magnetic-field model, the program calculates total drift velocities ($\underset{\sim}{E} \times \underset{\sim}{B}$ + gradient + curvature) for plasma-sheet particles. Specifically, it computes the motion of the inner edge of each species k of the plasma-sheet electron-ion distribution, namely five "energy invariants" for electrons, and ten for singly-charged positive ions.

Loss of electrons by precipitation is included in the present model by making a conventional assumption, namely that the electrons suffer strong pitch-angle scattering. Under these conditions, the inner edge of the electron plasma sheet is often essentially a precipitation boundary [Vasyliunas, 1968; Kennel, 1969]. We include erosion of the electron plasma sheet's inner edge in an approximate way that involves having the computer keep track of two boundaries for each energy invariant: one boundary where 25% of the electrons have been lost, another where 75% have been lost. Proton loss has been ignored in this first set of runs.

Given the velocities of different components of the inner edge, the program advances the position of the inner edge for each component by the amount appropriate to one time step δt (30 seconds in these runs) by solving equation 2. This closes the logical loop for another time step, and so on.

In the actual numerical procedure, the program, in every time step, reinterpolates the magnetic field model, recalculates Birkeland currents for the new particle and magnetic-field configuration, reads the observed electron fluxes, readjusts Pedersen and Hall conductivities, readjusts the polar boundary potential drop, re-solves the two-dimensional elliptic equation for ionospheric potentials using a 21 x 28 grid, reinterpolates the mapping to the equatorial plane, calculates corotation, curvature and gradient drifts, recomputes boundary velocities and moves the inner edge of various components of the plasma-sheet (which we represent by 400 boundary points).

The problem is further complicated by the fact that the inner edge of the plasma sheet is often rather thin (of the order of one grid spacing). Electric fields can vary by large factors through this edge region and often change sign. In other words, electric fields generated by one part of the inner edge strongly affect particle motions in other parts. To accurately model this sub-grid-scale phenomenon, we have had to include a rather intricate self-correction scheme, which substantially complicates the program.

III. DESCRIPTION OF THE EVENT

A. Basic description of the event

In the long process of choosing an event to model, we had to scan many data bases for the years 1975-1976. The following criteria were used (some of them somewhat contradictory):

a) A typical and clearly defined substorm (with one major expansion and recovery) so that our simulation model would be as general as possible.

b) Long enough duration so that we could have several passes of polar-orbiting satellites during the course of the substorm, in order to maximize available observations of electric fields, magnetic fields, and auroral particles. (This partly contradicts criterion a).

c) Good electric-field data from several passes (before, during and after the substorm). Several passes must be roughly dawn-dusk or dusk-dawn to allow accurate estimation of the cross-polar-boundary potential.

d) As many good DMSP images of the aurorae as possible.

e) Being close to equinox (to minimize difficulties with our untilted magnetic field model).

f) North America being at nighttime so that we can make maximum use of North-American ground magnetometers. This implies a UT restriction.

g) A date that was as early as possible so that the data could be processed and supplied to us.

h) Availability of other magnetospheric and ionospheric data (to be used in future detailed analysis of the event).

i) Positioning of a satellite near the inner edge of the plasma sheet.

The substorm we finally chose satisfied criteria b, c, e, f, g and partly satisfied criteria a, d and h.

Figure 3 (top panel) shows the Fort Churchill magnetogram for 19 September 1976 as a function of Universal Time (Greenwich Mean Time). The event we have chosen to model is the one with an onset at 1000 UT and a duration of about 5 hours; at onset Fort Churchill was at 1455 MLT. A small disturbance was observed a few hours earlier (around 0600 UT); unfortunately, two of the S3-2 satellite passes occurred during that time span.

Further investigation of auroral and mid-latitude magnetograms reveals that there was more than one substorm in the time span of our simulation. Virtually all nightside stations show a large substorm with onset at about 1000 UT or shortly thereafter, but some stations (e.g. College and Pacific Ocean stations) show a smaller localized expansion at 1150 UT. We cannot even rule out the possibility of additional minor and localized disturbance. Our method of computing conductivities and the boundary potential drop, based on discrete satellite passes, cannot resolve these small recoveries and expansions. Therefore we computed the response of the inner magnetosphere to one substorm with a long, slow recovery although it appears that the actual situation was considerably more complex.

B. Satellite data

The primary satellite used for the ionospheric electric field was the Air Force's S3-2 satellite. This satellite is a spin-stabilized

polar orbiter, inclination 97°. It has two dipole electric-field probes, one in the spin plane, which is nominally the orbital plane, and one along the spin axis. It also has a tri-axial, fluxgate magnetometer and an energetic electron detector. Data were stored on an onboard tape recorder. Coverage of data was limited by the relatively few tracking stations available to transmit the data.

Figures 4-6 present electric fields, magnetometer and electron-energy-flux data from the S3-2 satellite for 3 passes during the event. (For further discussion of the processing of the data, see Burke et al [1979]).

The component of electric field in the forward direction of the satellite and approximately perpendicular to the magnetic field is shown in the bottom panels of Figures 4-6. The conventional polar cap potential drop (boxes in Fig.3, bottom) was obtained by integrating $\underset{\sim}{E} \cdot d\underset{\sim}{l}$ across the polar-cap (from reversal to reversal). As is obvious from Figures 4-6, the polar cap boundary is sometimes hard to determine; the most equatorward reversal was generally used (arrows in Figures 4-6). The middle panel of Figures 4-6 show the magnetic variations, ΔB along the spin axis of the satellite, which was almost exactly east-west. It is apparent that region-1-type currents often extended well into the sunward convection region (denoted by vertical lines, e.g. 1134 UT in Figure 6). Thus the "polar boundary potential drop", from the viewpoint of our model (lines with error bars in Figure 3b), is often significantly smaller than the conventional polar cap potential drop.

Figures 4-6 are significant in that they are among the first satellite data across the polar cap showing simultaneous ΔB perturbations and electric field data. These data reveal some interesting features: there is a general correlation between the magnitude of the transverse magnetic field perturbation ΔB and the forward component of electric

field. Simultaneous measurements of particles and magnetic fields on the ISIS 2 satellite during quiet times were found to be correlated [Burrows et al., 1976; Klumpar et al., 1976; and McDiarmid et al., 1977, 1978]. McDiarmid et al. [1978] further compared magnetic perturbation profiles with average electric field profiles reported by Heppner [1972] and Gurnett [1972] and found the shapes to be very similar, suggesting that the magnetic field tilts in the direction of the convection. However, in two of the passes presented here (Figures 5 and 6) regions of strong sunward convection are observed poleward of the strongest region-1 currents, suggesting that despite the general similarity, one cannot predict, at least during substorms, the plasma convection based entirely on ΔB, as suggested for steady-state conditions [McDiarmid et al., 1978].

The auroral region electric field and magnetic perturbation data in Figures 4-6 were used for comparison with theoretical results. Detailed discussion and comparison with theoretical predictions are presented in the following paper.

Also shown on Figure 5 are features of the Lockheed Ion Mass Spectrometer data from a nearly simultaneous S3-3 pass (R. D. Sharp, personal communication, 1977). The S3-3 pass was also dawn-dusk, from an invariant latitude of 61.6°, magnetic local time of 1805 at 1005 UT, to an invariant latitude of 54°, magnetic local time of 0730 at 1100UT. The S3-3 polar cap pass covered a much longer time span because of its higher altitude (which dropped from 7806 km to 2704 km during this time period). Despite minor differences in MLT and UT between S3-2 and S3-3, the electron fluxes observed at corresponding invariant latitudes were remarkably similar. In particular, precipitating electron bursts

resembling "inverted V's" were observed near 68°, 69°, 74°, and 77° invariant from both satellites. In the S3-2 data, these bursts were associated with upward field-aligned currents; in the S3-3 data, these bursts were associated with upward flowing ions. Thus it seems reasonable to infer a connection between upward flowing ions and upward Birkeland currents. It is reassuring to note that no upward flowing ions were observed in our modeling regions (not even in the upward current region on the dawnside), since upward flowing ions may be associated with parallel electric fields [Shelley et al., 1976; Mizera and Fennell, 1977; Ghielmetti et al., 1978], and we have assumed no parallel electric fields in our modeling region.

IV. INPUT

A. Polar boundary potential distribution

The polar-boundary potential drop is, in our view, the most important single input parameter to our model. The potential drop is our monitor of the solar wind and boundary layer's influence on the inner magnetosphere. It should be emphasized that we have taken our polar boundary at the equatorward edge of the region-1 current, in contrast with the more conventional polar cap defined by the electric field reversal (see Figure 3, bottom).

Measurements shown in Figure 3 (bottom) indicate that the potential drop is relatively constant prior to onset, and increases during the growth and main phases of the substorm. (Such an increase was also suggested by Mozer [1973], based on balloon measurements). However, as a result of the data points being so far apart it is difficult to derive a "best fit" curve. The curve we have chosen is shown in solid line in Figure 3 (bottom panel). The potential drop was kept constant at 20 kV utill 0900 GMT. Then we increased it linearly to reach a peak of 80 kV at 1050, after which it stayed constant throughout the long recovery phase of our model substorm.

As a result of the uncertainty in the time dependence of the polar boundary potential drop, we ran our program again with a different assumption about the potential drop (dotted line), with a peak value of 140 kV. Detailed comparison with data shows the smaller potential drop to be more realistic.

In addition, the following difficulties were encountered trying to derive a potential drop as a function of time during the event:
(i) Although most of the passes were mainly dawn-dusk, some only "skimmed" the polar cap boundary (in particular the first two) giving rise to an error (probably an underestimate) in the resulting potential drop.
(ii) We have no potential-drop measurements between 0640 and 0940 GMT. Combined with the fact that the 0450 and 0620 GMT passes were during the small disturbance and were therefore ignored, we had virtually no data between 0450 and 1000 (onset). As a result we believe that we may have underestimated the length of the growth phase for this run, represented by the solid curve in Figure 3 from 0900 to 1000 GMT.

Given the potential drop, we apply a simple analytic function to estimate the potential distribution on the polar boundary. The electric equipotential curves were compressed across the dayside in accordance with observations [Heelis et al., 1976]. The polar boundary was assumed to be an offset circle [e.g., Feldstein, 1973; Meng et al., 1977]. We have chosen an offset of two degrees toward midnight, away from the geomagnetic pole. The results of the first simulation suggest that our results can be improved considerably by a more judicious choice for the fit to the polar boundary potential distribution.

B. Magnetic field model

For these simulation runs we used the analytic version of the Olson-Pfitzer [1974] magnetic field model. The model appears basically adequate for our purposes, although it has the disadvantage that typically $|\nabla \cdot \underline{B}| \sim 5\gamma/R_E$ on ring-current field lines. To the Olson-

Pfitzer analytic model, we added the magnetic field of a substorm current loop (see also section II), which is used to estimate the time-dependent magnetic field (and the resulting induction electric field) (Fig. 7). The loop was first suggested by Atkinson [1967] and used by McPherron et al. [1973] and many others. Our version of the loop has an equatorial eastward current across the tail at 50 R_E (representing interruption of the tail current during a substorm), Birkeland currents down to the northern and southern hemisphere ionospheres, westward electrojet, and another Birkeland current from the ionosphere out to the equatorial plane. For this first run, we chose the maximum current in the loop such that it would approximately reproduce the ground magnetic variation (positive bay) observed at Boulder. The loop was turned on at onset and reached its maximum value at 1040 UT (peak of the substorm) after which it gradually declined through the long model recovery phase.

Figure 8 shows contours of constant magnetic field in the equatorial plane for 0900 UT (an hour before onset). Although symmetric and dipole-like near earth, the contours deviate from this symmetry for larger L values. The contours for $L < 6$ will be essentially the same even later in the event, when the substorm loop is at full strength. For larger L values, the contours near midnight are pulled antisunward, representing return to a more dipole-like structure near midnight.

C. Conductivity Model

The conductivity model is an important input to the equation for conservation of ionospheric current (equation 4 in section II), which we solve numerically to find the potential distribution in the ionosphere. The height-integrated Pedersen and Hall conductivities include base-level

and time-dependent terms. The base-level term includes day-night asymmetry and solar-zenith-angle dependence. Nightside midlatitude values are estimated from Rowe and Mathews, [1973] and roughly agree with Harper and Walker [1977]; dayside conductivities are consistent with Harper [1977].

To estimate the spatial dependence of the auroral enhancement in an accurate way, for the whole auroral zone, one would need global measurements of electron density or global measurements of the flux of auroral electrons incident on the ionosphere. Such measurements are, of course, not available, and one must either approximate or extrapolate available data. Our present conductivity model is a first attempt at including these enhancements in a time-dependent way.

The primary method we have used to estimate height-integrated conductivities for the 19 September event involves an empirical formula that we derived, relating height-integrated Pedersen and Hall conductivities to auroral electron energy flux and mean electron energy. M.H. Rees and his collaborators [Jones and Rees, 1973, and Rees, private communication] have calculated electron-density profiles in the night-time auroral ionosphere for various energy fluxes and mean energies, and for assumed neutral-atmosphere models. Using standard formulas for Pedersen and Hall conductivities [Rishbeth and Garriott, 1969], we deduced height profiles of Hall and Pedersen conductivities for three of Rees' models. We then numerically integrated these over height and fitted the results to simple power laws, with the following results:

$$\Delta\Sigma_p = (5.2 \text{ mhos}) \left[\frac{\text{Energy Flux}}{\text{erg/(cm}^2\text{sec)}}\right]^{1/2} \qquad (9)$$

$$\Delta\Sigma_H = 0.55 \left[\frac{\text{Average Electron Energy}}{1 \text{ kev}}\right]^{0.6} \times \Delta\Sigma_p \qquad (10)$$

Energy flux and average electron energy were computed from S3-2 electron data, using 32 electron channels that cover the range .08-17 keV.

For our substorm simulation we used flux measurements from four passes on 19 September 1976: 0400, 1000, 1150, and 1500 GMT. For each pass we determined the flux as a function of invariant latitude.

We have constructed conductivity models with two different degrees of latitudinal smoothing at the inner edge of the plasma sheet (Table 2). The smoothing is necessary because of the inability of the current conservation difference equation to cope with very sharp conductivity jumps. For a detailed numerical description of the conductivity model, see section V.

Figure 9 demonstrates the latitudinal dependence of our conductivity model for these "less smooth" conductivities. We plot, for a given time (1150 UT), the Pedersen and Hall conductivities as a function of local time for 4 different latitudes. Note the conductivity peaks at local noon except for the 70° profile when the auroral enhancement causes the conductivity to peak on the night side.

Figure 10 shows the universal time dependence of the conductivity model. We plot the Pedersen conductivity profile at auroral zone latitude (70°) for various phases of the substorm. The conductivity peak coincides with the peak in the cross-polar-cap potential drop (at 1150 UT).

D. Initial hot-particle distribution in the magnetosphere

The initial plasma configuration that we assumed is somewhat arbitrary, since no magnetospheric hot-plasma data were available. The inner edge of the plasma sheet was assumed to have a finite thickness (about 0.7 R_E) and was located at L ≈10. An isotropic pitch angle distribution was assumed with n_e = 0.9 cm^{-3} , kT_e = 1.5 keV and kT_i = 4.5 keV at L ≈10. Unlike the other input parameters, these values were inserted once as initial conditions and were calculated at later times with the assumption that $\lambda_k = E_k (\int ds/B)^{2/3}$ serves as an adiabatic invariant (E_k = kinetic energy of particles of type k, $\int ds/B$ = flux tube volume).

V. NUMERICAL METHOD

The Earth's magnetosphere is, of course, an intrinsically three-dimensional system that cannot be realistically approximated as a two-dimensional system, uniform in the third dimension. One approach to the problem is therefore to attempt to solve the simultaneous time-dependent three-dimensional MHD equations. One group is attempting to do this [Lebouf et al., 1980]. Our approach has been to reduce the problem to a treatable two-dimensional computation by using the fact that the magnetic-field configuration in the inner magnetosphere can be estimated relatively accurately, and the field lines are relatively good conductors. In fact, we solve two 2-dimensional sets of equations (in the ionosphere and in the Earth's equatorial plane); the two regions are coupled via the geomagnetic field.

The system of equations (1 - 8) in section II.A describes the motion of the plasma sheet during disturbances and the resulting ionospheric currents and electric fields. Solution of the system of equations involves an intricate and elaborate numerical analysis. We therefore will describe only some of the most important aspects of the numerical treatments.

A. Coordinate System

In the ionosphere we have chosen an orthogonal 2-dimensional coordinate system (ξ,ψ) similar to the one described in Jaggi and Wolf

[1973]. The center of the coordinate system, however, is displaced 2 degrees toward midnight from the geomagnetic north pole (so that our polar boundary, which is shown in Figure 1b and is chosen to be independent of time, follows a contour of ξ = constant). A length increment ds in the ionosphere can thus be described as

$$ds^2 = \alpha^2 d\xi^2 + \beta^2 d\psi^2 \qquad (11)$$

where $\alpha(\xi)$ and $\beta(\xi)$ are some scalar functions. The resulting grid system (i,j) consists of 18 x 28 grid points covering all magnetic local times. The points are evenly spread in j with j = 3 or 31 at local noon, j $\approx$ 10 at dusk and j = 17 at midnight. The grid covers approximately the range $20° \lesssim \theta \lesssim 72°$ in colatitude. The latitudinal spacing of grid points $\alpha(\xi)\Delta\xi$ varies; in the main convection zone, $\alpha(\xi)\Delta\xi$ is equivalent to about 1.7°, while at mid- and low latitudes it varies from $\approx 1.8°$ to $\approx 8.7°$. The local-time grid spacing $\beta\Delta\psi$ is equivalent to about 0.86 hours.

The equatorial grid system is obtained by tracing magnetic field lines from ionospheric grid points out to the equatorial plane. This results in a nonorthogonal grid for the equatorial plane. The equatorial extent of our grid system is roughly $1.03 \lesssim L \lesssim 10$ and is somewhat time-dependent (since our magnetic field model is also time-dependent).

B. Inputs

Aside from the grid system various input parameters are needed to solve the time dependent system of difference equations that represent equations 1-8 in section II.A.

(i) Time Independent Inputs

For an isotropic pitch angle distribution, the distribution function is given by

$$f(\underline{v}) = \frac{n}{(2\pi\kappa T/m)^{3/2}} e^{-mv^2/2\kappa T} \qquad (12)$$

where n is the number density.

Using λ (the "energy invariant") and η (the "density invariant"), as defined in section II.A., one can derive

$$d\eta/d\lambda = \frac{2\eta_T \lambda^{\frac{1}{2}} e^{-\lambda/\lambda_{\kappa T}}}{\pi^{\frac{1}{2}} \lambda_{\kappa T}^{3/2}} \qquad (13)$$

where η_T is the total number of particles per unit magnetic flux in the flux tube and $\lambda_{\kappa T} = \kappa T(\int ds/B)^{2/3}$. We keep track of 15 distinct "species". For the electrons,

$$\lambda_k/q_k = 2579.3 \sinh [0.1925\ (k-6)] \qquad 1 \leq k \leq 5 \qquad (14)$$
$$\lambda_k = \lambda_{k-5} \qquad 6 \leq k \leq 10$$

and for the ions

$$\lambda_k/q_k = 317.0 \sinh [0.4\ (k-11)] \qquad 11 \leq k \leq 21$$

where λ is in units of eV $R_E^{2/3} \gamma^{-2/3}$; k is a running index and q_k is the particle's charge. We use two k values for each electron λ value, as part of our procedure for including electron loss by precipitation. (See subsection C.iii below.) The k = 11 species represents cold plasma. The resulting densities η_k are, for electrons,

$$\eta_k = \eta_T \left(\frac{280.1}{\lambda_{Te}}\right) \left(\frac{\lambda_k}{\lambda_{Te}}\right)^{\frac{1}{2}} \cosh[0.1925(k-6)] \exp\left[-\frac{\lambda_k}{\lambda_{Te}}\right] \qquad 1 \leq k \leq 5$$

$$\eta_k = \eta_{k-5} \qquad 6 \leq k \leq 10 \qquad (15)$$

and for ions

$$\eta_k = \eta_T \left(\frac{143.1}{\lambda_{Ti}}\right) \left(\frac{\lambda_k}{\lambda_{Ti}}\right)^{\frac{1}{2}} \cosh\ [0.4\ (k-11)] \exp\left[-\frac{\lambda_k}{\lambda_{Ti}}\right] \quad 11 \leq k \leq 21$$

The constant parameters are:

$$\eta_T = 1.7 \times 10^{21}\ \text{weber}^{-1}$$

$$\lambda_{Te} = 721\ eV\gamma^{-2/3} R_E^{2/3};\ \lambda_{Ti} = 2163\ eV\gamma^{-2/3} R_E^{2/3}$$

(ii) Time Dependent Inputs

a) Magnetic Field

The magnetic-field model at a given time t is described numerically by three matrices: B_e^{ij} ; R^{ij}; P^{ij}. For a given i, j ionospheric grid point, these matrices give the B_z and the polar coordinates, respectively, of the corresponding point in the equatorial plane (the mapping itself is done via the magnetic field). For the period before substorm onset, the matrices were calculated using the analytic version of the Olson-Pfitzer model [1974] to trace each grid point from its ionospheric origin to its equatorial crossing. For the peak of the substorm this field-line tracing procedure was repeated using a modified magnetic field that included the effect of the substorm current loop (see section IV.B). For other times, we interpolated between the "quiet-time" and the "substorm-peak" values of the three matrices. The flux tube volume was approximated using the formula

$$\left(\int \frac{ds}{B}\right)^{ij} \approx \left[B_e{}^{ij}/R^{ij} + 20\ (R^{ij})^{-1.3}\right]^{-1} \qquad (16)$$

b) Conductivity

Like Wolf [1970] and Jaggi and Wolf [1973] we adopt the

approximation of layer conductivity where

$$\Sigma_{\xi\xi} = \Sigma_p/\sin^2 I$$
$$\Sigma_{\xi\psi} = -\Sigma_{\psi\xi} = \Sigma_H/\sin I \qquad (17)$$
$$\Sigma_{\psi\psi} = \Sigma_p$$

where $\Sigma_{\xi\xi}$, $\Sigma_{\xi\psi}$, $\Sigma_{\psi\xi}$ and $\Sigma_{\psi\psi}$ are the components of the conductivity tensor in equation 7, Σ_p and Σ_H are height-integrated Pedersen and Hall conductivities, and I is the magnetic dip angle. (This approximation holds if we stay away from the geomagnetic equator). To calculate the height-integrated conductivities in mhos at grid point (i,j) at time t, we use the following formulas

$$\Sigma_p{}^{ij}(t) = \sum_{\text{hemispheres}} \left\{ 12.5\, S[\sqrt{\cos\chi^{ij}}\cdot u(\cos\chi^{ij})]+0.45 + \Delta\Sigma_p{}^{ij}(t) \right\} \qquad (18)$$

$$\Sigma_H{}^{ij}(t) = \sum_{\text{hemispheres}} \left\{ 18.75\, S[\sqrt{\cos\chi^{ij}}\cdot u(\cos\chi^{ij})]+0.15 + \Delta\Sigma_H{}^{ij}(t) \right\} \qquad (19)$$

In each formula, the first term represents the time-independent sunlight effect, χ^{ij} = solar-zenith angle at (i,j), computed assuming that the earth's magnetic dipole is perpendicular to the earth-sun line; u(x) = 1 or 0 depending on whether $x > 0$ or $x \leq 0$; and S represents a numerical function that tries to smooth slightly the sharp jumps at dawn and dusk. The second terms in (18) and (19) give base-level nightside values. The third terms represent time-dependent auroral enhancements; they were computed in a complicated way from (9) and (10), which give the enhancements below the S3-2 satellite, by linearly interpolating in universal time to get values for times t between satellite passes, extrapolating smoothly in local time assuming twice as great enhancement

at midnight as at noon, converting from actual GM latitude to an effective model latitude, and smoothing latitudinal fine structure.

c) Polar boundary potential distribution

S3-2 satellite measurements were used to estimate the dawn-dusk potential drop across the polar cap (see, e.g., Figure 4-6). The time dependence was approximated, again, by linear interpolation (Figure 3b). The longitudinal dependence was chosen so as to concentrate the potential drop across a smaller distance on the dayside (the "throat" region [Heelis et al., 1976]) than on the nightside.

The boundary potential is given by

$$
\begin{aligned}
V_b &= V_o \sin 2\psi && \text{near noon } (\psi \leq \pi/4 \text{ or } \psi \geq 7\pi/4) \\
V_b &= V_o && \text{for } \pi/4 < \psi < \pi/2 \\
V_b &= V_o \sin\psi && \text{for the night sector } (\pi/2 \leq \psi \leq 3\pi/2) \\
V_b &= -V_o && \text{for } 3\pi/2 < \psi < 7\pi/4
\end{aligned}
\qquad (20)
$$

where V_o = 1/2 x (cross polar boundary potential drop).

C. Calculations of electric fields and plasma motion

Our general approach to the solution of our problem is schematically shown in Figure 2 and discussed in section II.B. In order to complete a time step in our logic loop we have to solve, simultaneously, equations 1-8. We split this task into 3 parts: calculation of the potential distribution V in the ionosphere (equation 7); calculation of the electric field at an arbitrary point and calculation of the plasma sheet motion (equation 2).

(i). Calculation of the potential matrix V

The electrostatic potential V is computed using the conservation law

for ionospheric currents (equation 7). Once we compute the horizontal conductivity and the Birkeland currents we approximate equation 7 numerically by

$$V^{ij} = \sum_{\ell=1}^{4} C_{\ell}^{ij} \; V^{i_\ell j_\ell} + C_5^{ij} \tag{21}$$

where $(i_\ell, j_\ell) = (i+1,j)$, $(i-1,j)$, $(i,j+1)$ and $(i,j-1)$, respectively, for $\ell = 1, 2, 3, 4$. The factors $C_1 - C_4$ are the same as given in Jaggi and Wolf [1973], and C_5^{ij} is given by

$$C_5{}^{ij} = \sum_k C_{5k}^{ij} = \sum_k \left\{ -\sum_{\ell=1}^{4} C_\ell{}^{ij} \Delta V_{\ell k} + \Delta V_{ok}{}^{ij} \right\} \tag{22}$$

The present case is different from the case presented in Jaggi and Wolf [1973] in that many "species" are now considered (running index k over 21 "species"). The term $\Delta V_{\ell k}$ = amount by which the potential at (i_ℓ, j_ℓ) is changed due to presence of discontinuity k, and $(i_o, j_o) \equiv (i,j)$. As discussed later, the sum includes only layers that cut the "cross", namely the lines connecting (i,j) to the (i_ℓ, j_ℓ), $\ell = 1,\ldots,4$. We find that

$$\Delta V_{\ell k} = \frac{1}{2} L_{\ell k} \left[\frac{j_{\parallel ik}}{\Sigma_{\xi\xi} \cos^2\zeta + \Sigma_{\psi\psi} \sin^2\zeta} \right] \tag{23}$$

plus a constant that does not depend on ℓ and eventually cancels out. Here $L_{\ell k}$ = perpendicular distance from inner edge k to grid point (i_ℓ, j_ℓ), $j_{\parallel ik}$ = Birkeland current coming down into the ionosphere along

the inner edge for species k, per unit length along the inner edge, and ζ= angle between the inner edge and the i = constant grid line. (Equation 23 is based on the assumption that the conductivity, and the electric field due to a layer,is approximately constant over the order of a grid spacing). Substituting equation 23 into equation 22 gives

$$C_5{}^{ij} = \frac{1}{2} \sum_k \frac{j_{\parallel ik}}{\Sigma_{\xi\xi}\cos^2\zeta + \Sigma_{\psi\psi}\sin^2\zeta} \left[-L_{ok} + \sum_{\ell=1}^{4} C_\ell{}^{ij} L_{\ell k}\right] \qquad (24)$$

One problem here is that in computing the ΔV's, we neglected conductivity inhomogeneities. It turns out to be better in the formula for C_5 to also neglect the conductivity-gradient terms in the C_ℓ's, namely to make the following replacements, using the notation of the Jaggi-Wolf paper:

$$C_5{}^{ij} = \frac{1}{4} \sum_k \frac{j_{\parallel ik}}{\Sigma_{\xi\xi}\cos^2\zeta + \Sigma_{\psi\psi}\sin^2\zeta} \left\{ -2L_{ok} + \frac{\frac{b^{ij}}{\Delta\xi^2}(L_{1k}+L_{2k}) + \frac{a^{ij}}{\Delta\psi^2}(L_{3k}+L_{4k})}{\frac{b^{ij}}{\Delta\xi^2} + \frac{a^{ij}}{\Delta\psi^2}} \right\} \qquad (25)$$

The quantity in curly brackets can be shown to be exactly zero for any edge that fails to cut the cross, assuming a straight boundary and equal grid spacing, and thus we can self-consistently consider the sum to be restricted to species values whose inner edges cut the cross.

The sum in (25) is a numerical approximation to an integral over energy invariant λ. Ideally, we would have enough species k that many k-values would break the cross and contribute to the sum for any (i,j). If the spacing between inner edges of different k happens to be large, then the sum for a given (i,j) may be a poor approximation to the

corresponding integral over λ for that (i,j). To take account of this problem, we define I_{layer} subspecies between each pair of successive k-values (species) and attribute to each subspecies' inner edge an interpolated position and a reduced and interpolated subspecies $j_{\|}$. Subspecies are labeled by the index k'. The sum in (25) then becomes a sum over subspecies k'. The choice of I_{layer} is discussed in subsection E.

The difference equation (21), representing equation 7 in section II.A, is solved by a straightforward iterative technique (see also Jaggi and Wolf [1973]). For a given time t, we derive the boundary potential V^j on the polar boundary, as described in subsection B.ii.c. Given the boundary condition $j_\xi = 0$ at the equatorward edge (lat. $\approx 21°$), given a set of values V^{ij} as a "guess" and computing the coefficients $C_1{}^{ij} - C_5{}^{ij}$, we obtain an improved set of values $(V')^{ij}$ as follows:

$$\delta V^{ij} = W[C_1{}^{ij} V^{i+1,j} + C_2{}^{ij} V^{i-1,j} + C_3{}^{ij} V^{i,j+1} + C_4{}^{ij} V^{i,j-1} + C_5{}^{ij} - V^{ij}] \quad (26)$$

$$(V')^{ij} = V^{ij} + \delta V^{ij} \quad (27)$$

where W is a weight factor ($0 < W \leq 1$). This procedure is repeated many times until

$$\sum_{i,j} |\delta V^{ij}|^2 \leq \varepsilon \quad (28)$$

Provided the initial guess is good, criterion (28) is satisfied within ~50 iterative steps. We should comment that this simple iteration scheme is efficient because we have a very good initial guess for V each time step, based on V for the last two time steps.

(ii) Calculation of the electric field

The simplest and most straightforward manner of computing the

electric field at an arbitrary point is, of course, to use some form of interpolation based on the potentials V^{ij} at the grid points. This method, however, will not suffice in the region of the "inner edges" due to the large electric-field discontinuities at some inner edges. We thus developed a more intricate and complex method of computing the electric field.

To calculate motions of the inner edges, we must do accurate computations of electric fields at noninteger i-values, which we label I. We start from an interpolation formula, then correct it for sharp inner edges. To compute the two components of ∇V at the point (I,j), where $i < I < i+i$, we use the following formulae:

$$\frac{\partial V}{\partial I}(I,j) = \frac{1}{2}\,[V^{i+1,j} - V^{i-1,j}] + (I-i)[V^{i+1,j} - 2V^{i,j} + V^{i-1,j}]$$

$$+ \sum_{k'} \{\frac{\partial \Delta V_{k'}}{\partial I}(I,j) - \frac{1}{2}\,[\Delta V_{k'}{}^{i+1,j} - \Delta V_{k'}{}^{i-1,j}] - (I-i)[\Delta V_{k'}{}^{i+1,j} - 2\Delta V_{k'}{}^{i,j} + \Delta V_{k'}{}^{i-1,j}]\} \tag{29}$$

$$\frac{\partial V}{\partial J}\,(I,J)\Big|_{J=j} = \frac{1}{2}[V^{i,j+1} - V^{i,j-1}] + (I-i)\,[V^{i+1,j+1} + V^{i,j} - V^{i,j+1} - V^{i+1,j}]$$

$$+ \sum_{k'} \{\frac{\partial \Delta V_{k'}(I,J)}{\partial J}\Big|_{J=j} - \frac{1}{2}\,[\Delta V_{k'}{}^{i,j+1} - \Delta V_{k'}{}^{i,j-1}] - (I-i)[\Delta V_{k'}{}^{i+1,j+1} + \Delta V_{k'}{}^{i,j}$$

$$- \Delta V_{k'}{}^{i,j+1} - \Delta V_{k'}{}^{i+1,j}]\} \tag{30}$$

Here and later in the paper, we use I and J for non-integer values of the grid indices i and j. The first lines of (29) and (30) give a straightforward interpolation formula. In each second line, the first terms give the appropriate component of the potential gradient generated by each inner edge k'. The rest of each second line and third line subtracts off the interpolation-formula result for the potential gradient. Thus each curly-bracketed term gives the difference between the potential gradient at (I,j) due to inner edge k' and the approximation to that potential

by (23), is proportional to the distance from grid point (i,j) to inner edge k' and to the Birkeland current per unit length along inner edge k' as it crosses grid line j. The curly-bracketed correction terms in (29) and (30) are zero if the point (I,j) and all the relevant grid points lie on the same side of inner edge k'.

(iii). Plasma Motion

The inner edge of a given species k is specified by $a_k^j(t)$, where j is our local time index, which varies between j = 3 and j = 30. That is, we use the point where the inner edge k crosses the j = integer line (these are lines of ≈ constant longitude). In most cases, the inner edges tend to run almost parallel to lines of constant latitude. Our task is to compute $\partial a_k^j(t)/\partial t$.

The basic formula for drift velocity of particles $\underset{\sim}{E} \times \underset{\sim}{B}$ drifting in a potential electric field and also gradient and curvature drifting (assuming isotropic pitch angles) is the following:

$$\underset{\sim}{v}_D = \underset{\sim}{B} \times \nabla V_{eff}/B^2 \tag{31}$$

where V_{eff} includes the convection potential, the corotation potential and the effects of gradient and curvature drifts (see equations 2 and 3 in section II.A). If we now apply this formula to the ionosphere and use it to calculate the rates of change of i and j coordinates due to drift, we find

$$\frac{dI}{dt} = \frac{\partial V_{eff}}{\partial J}(\alpha\beta\Delta\xi\Delta\psi|B_{ir}|R_E^2)^{-1} \tag{32}$$

$$\frac{dJ}{dt} = -\frac{\partial V_{eff}}{\partial I}(\alpha\beta\Delta\xi\Delta\psi|B_{ir}|R_E^2)^{-1} \tag{33}$$

where B_{ir} = radial component of B at the ionosphere. In deriving these formulas, we have had to take into account the fact that the magnetic field is not exactly perpendicular to our ionospheric grid, which lies on a spherical shell. The rate of change of the i-value of the intersection of layer k with grid line j is given by

$$\frac{\partial a_k^j}{\partial t} = \frac{dI}{dt} - \frac{dJ}{dt}\frac{\partial a_k^j}{\partial J}$$

$$= \left[- \frac{\partial V_{eff}}{\partial J} - \frac{\partial V_{eff}}{\partial I}\frac{\partial a_k^j}{\partial J} \right] (\alpha\beta\Delta\xi\Delta\psi|B_{ir}|R_E^2)^{-1} \quad (34)$$

Equation 34 does not adequately describe the motion of electrons because it does not include electron loss due to pitch angle scattering. In most simple models, loss of plasma-sheet particles by precipitation or charge exchange increases rapidly as the flux tube approaches the earth and becomes smaller in volume. Thus the loss process tends to erode the inner edge of the plasma sheet. We estimate the erosion of the electron plasma sheet by keeping track of two electron inner edges for each λ, one representing 25% loss and the other 75% loss.

For strong pitch angle scattering one can estimate the precipitation life time τ as

$$\frac{1}{\tau} = \frac{\text{[Flux of particles out of flux tube]}}{\text{[Flux tube content]}} = (2\lambda/m)^{1/2}(2|B_{ir}|)^{-1} \times (\int ds/B)^{-4/3} \quad (35)$$

Given τ we approximate the electron inner edge erosion by

$$\left(\frac{\partial a_k^j}{\partial t}\right)_{erosion} = - 0.607 \left(\frac{a_k^j - a_{k+5}^j}{\tau_k^j}\right) \qquad 1 \le k \le 5, \text{ 75\% precipitated} \quad (36)$$

$$\left(\frac{\partial a_k^j}{\partial t}\right) = - 1.82 \left(\frac{a_{k-5}^j - a_k^j}{\quad}\right) \qquad 6 \le k \le 10, \text{ 25\% precipitated}$$

The inner-edge motion for electrons is obtained by adding the rates given in (34) and (36).

We must now convert (34) and (36) to a form suitable for numerical solution, and first discuss the numerical method for stepping along in time. The method we have chosen is the simplest first-order one:

$$a_k^j(t+\Delta t) = a_k^j(t) + \frac{\partial a_k^j}{\partial t}(t)\,\Delta t \qquad (37)$$

More accurate and intricate numerical methods for stepping along in time, such as second-order Runge-Kutta and a second-order predictor-corrector method, were considered. The simpler scheme (37) was used because it was much easier to incorporate into our complex program, and because analysis showed it equal or superior to the more complicated method with regard to stability of short-wavelength ripples of the inner edges. Flute-type ripples physically should decay exponentially, especially rapidly in low-conductivity regions. However, if the time step is long compared to the physical decay time, the system becomes numerically unstable, for any of the numerical methods we tested, and it is the requirement of stability against boundary ripples that limits our time step. The more complicated numerical methods could not improve on (37) with regard to maximum allowed time step. For time steps short enough to satisfy the stability requirement, the additional accuracy of the higher-order methods proved unimportant.

We should mention that, in order to eliminate a numerical instability that tends to ripple inner edges on the night side, we do not use (37) to compute $a_k^j(t + \Delta t)$ for every j-value. Instead, for even

j-values on the night side, we compute $a_k^j(t + \Delta t)$ by linearly interpolating between the $a_k^j(t + \Delta t)$ values for odd j.

D. Accuracy tests

The complexity and the size of our numerical system make it difficult to evaluate the error in many conventional ways. We therefore tried to estimate and minimize the error by examining the dependence of the results on the values of various numerical-analysis parameters.

The essential numerical-analysis parameters in our program are the following: $\Delta t, \Delta\xi, \Delta\psi, k_{max}, I_{layer}, \varepsilon$ and W. We test accuracy by varying each parameter separately. The difference equations represent the differential equations exactly in the following limits: $\Delta t, \Delta\xi, \Delta\psi, \varepsilon \to 0$ and $k_{max} \to \infty$.

As mentioned in section IIC we have used $\Delta t = 30$ sec as a constant time step throughout the event. We found that taking a significantly longer time step results in oscillatory instability. Tests run earlier have shown that choosing substantially smaller Δt causes negligible change in the results.

We also have built-in means for testing accuracy by doubling $\Delta\xi$ and $\Delta\psi$, as defined in equation 11. We found that doubling the grid spacing did not change the results in a major way, although details were, of course, lost.

The parameter k_{max}, the number of particle species whose motions are computed in detail, was not varied from its chosen value 21, because that number of species seemed to provide the desired energy resolution. However, the program was run for various values of I_{layer}, i.e., various numbers of subspecies interpolated in between the k_{max} species whose

motion we follow in detail (section V.C). Results for $I_{layer} = 1$ and $I_{layer} = 9$ differed negligibly, and we therefore chose $I_{layer} = 1$.

The convergence criterion ε defined by (28), was set equal to 10^3 volt^2. Test runs with smaller ε-values produced insignificantly different results. The weighting factor W, defined by (26), was set equal to 0.5, close to the largest value for which the interation scheme consistently converged.

E. Numerical problem near local noon

The present numerical method has a deficiency near local noon. Since we assign, for a given particle species and a given local time, only one i-value for the inner edge, we cannot have a "ring current wrap-up" which will occur in reality when a species of particles attempts to form a complete ring current. The problem becomes apparent near local noon (see e.g. Figure 4 in paper 2) for the high energy ions, which are prevented from forming a ring. In general this problem could not be overcome using the present numerical method and we therefore stopped the simulation at 1300 UT. However we did "prevent" the particles from going to infinity near local noon by holding them at $\sim$ 10.5 R_E if the electric field indicated a sunward motion in this region.

VI. OVERVIEW OF RESULTS

A. Survey

This section is devoted to a survey of numerical results from our substorm simulation. More results, analysis and comparison with data are presented in paper 2 and paper 3. (See also Harel et al., [1979].)

Four computer runs were performed covering the four hour span from 0900 UT (an hour before onset) to 1300 UT (well into the recovery phase). Table 2 summarizes those runs.

The first run has a peak polar-boundary potential drop of 80 kV (following the solid line in Figure 3). The conductivity model for this run, although including a smoothing function at the plasma's inner edge, was less smooth than the other three. Induction electric fields were estimated by means of our fictitious substorm current loop (Figure 7) turned on at onset (see Section IV.B).

Run 2 was similar to the first run with the exception of a minor numerical method correction and a greater smoothing of the conductivity. By comparing these results with run 1 we can learn the effect of the conductivity smoothing on the numerical results.

The third run is similar to the second except that it omits the substorm current loop. For this run, the magnetic field model was time-independent, in order to evaluate the effect of the induction electric field on plasma motion.

Run 4 was performed with an estimated potential drop of 140 kV at 1150 UT (dashed curve in Figure 3). Further analysis indicates that we considerably overestimated this peak potential drop.

We believe run 1 to be the most realistic because of its sharper conductivity gradients and 80 kV peak potential drop; therefore most of the results presented here and in the following two papers were obtained from that run.

In order to be as independent as possible of initial conditions, we actually started all 4 runs at 0700 UT (two hours prior to the beginning of the growth phase). From past experience we found that in two hours, magnetospheric time and for a 50 kV cross-polar-boundary potential drop, the plasma configuration and electric fields reaches near-equilibrium almost regardless of initial conditions [Harel and Wolf, 1976], provided the particles were initially put at $L \gtrsim 8$. However, with the present 20 kV potential drop, the process is slower and the system progresses only part-way toward equilibrium.

Figure 11 describes our assumed initial configuration in the equatorial plane of the magnetosphere. Inner edges of 3 sample particle species are also plotted (symmetric and initially placed at $L \gtrsim 10$). Equipotential lines 6 kV apart are plotted in the rest frame of the rotating earth. The electric-field pattern is distorted because our arbitrarily assumed initial particle distribution implied intense localized partial ring currents and thus large ionospheric currents and electric fields.

Figure 12 shows the potential pattern at 0900 after the initial 2 hours' "quiet time" polar boundary potential drop. As expected, the plasma sheet drifted in sunward, as described by the 3 sample "inner edges" at $L \gtrsim 8$. The outer circle represents the mapping of our polar boundary to the equatorial plane. Note the extensive electric field

shielding equatorward of the inner edges, especially on the nightside; (see also Jaggi and Wolf [1973]).

Figure 13 shows the electrostatic potential distribution for 0900 as viewed from above the north-polar ionosphere. The equipotential curves shown in Figure 11 are here plotted in the ionosphere. Curve I, representing our assumed "polar boundary", is an offset circle centered 2 degrees from the north pole toward midnight. Shielding is obvious again equatorward of the particles' inner edges ($\sim 60^{\circ}$). The polar cap region inside of curve I (mapped to the region outside of this curve in the equatorial plane in Figure 12 and the following figures) is not included in our model. Therefore, electric field and particle results shown in this region are merely extrapolations.

Figure 14 shows the potential contours including the Earth's corotation potential for the same universal time (0900). The earth's corotation field dominates for $L < 5$, represented by nearly circular equipotentials, but falls off at larger L values where the potential pattern is similar to Figure 12. The boundary between the two regions is the "saddle point equipotential" (termed later an Alfvén layer) of -15.4 kV.

The next group of figures is a survey of some of the results from our main run (run 1 in table 2). Figures 15-19 show equatorial potential contours in the rest frame of the rotating earth and inner edge locations at 1000- ε UT, 1000+ ε (onset), 1050 (highest observed potential drop) and 1300 (partial recovery) (Figure 3). Two features are most obvious:

(i) Injection. As time progresses, plasma sheet particles are injected sunward and around the flanks to form an asymmetric partial ring current

at $L \tilde{>} 5\text{-}8\ R_E$. Although others [e.g., McIlwain [1974], Roederer and Hones [1974], Smith et al. [1979]] have reproduced ring formations, their models, unlike ours, do not include self-consistent electric fields that both affect and are affected by plasma motion. As time progresses, the inner edge of the high energy ions drifts inward toward earth at dusk faster than low energy ions and all electrons, giving rise to dispersion relations at synchronous orbit similar to those reported by DeForest and McIlwain [1971]. (For a more detailed discussion, see paper 2). These results point in favor of the conventionally assumed mechanism for the formation of the main-phase ring current: the inner edge of the plasma sheet is driven inward from the tail to produce a ring current with the observed particle dispersion. For more discussion of this point, see Wolf and Harel [1979].

(ii) Shielding. Although the cross-polar-boundary potential drop increases to a value of about 80 kV, most of the electric field is concentrated outside of the most equatorward inner edge with some leakage to the lower L shells. By 1300 (Figure 19), shielding of the near-Earth region is quite effective. In our case the shielding is done mostly by plasma-sheet ions, since most of the electrons are lost by strong pitch-angle scattering [Southwood and Wolf, 1978]. There also seems to be a dawn-dusk asymmetry in the electric field. Whereas on the dawn side, electric fields decline smoothly with decreasing latitude, on the dusk side, the strongest poleward electric fields generally occur well equatorward of the polar-cap boundary. (For further discussion and comparison of predicted and measured electric fields, see paper 2).

Figure 20 shows the total electric field in the equatorial plane at

1300. While the corotation field dominates at L < 4 because of the earth's rotation and shielding of the potential electric field by the plasma sheet's inner edge, the dawn-dusk convection field dominates at large L values. Induction fields, although included, are very small with the exception of the westward component in the region near local midnight.

The resulting $\underset{\sim}{E} \times \underset{\sim}{B}$ velocity flow field is shown in Figures 21 and 22. The arrows show the instantaneous velocity of cold plasma particles in the equatorial plane (Figure 21) and mapped into the ionosphere (Figure 22). At 1800 local time, we can see the flow reversal from corotation to sunward convection occurring at about 65° invariant latitude.

Figures 23-26 show contours of constant equivalent potential $V\text{-}V_{corotation}+(\lambda/q)(\int ds/B)^{-2/3}$ for various λ's and various times. The λ's are "energy invariants" of the motion of various type particles and are defined in equation 1. The particle thermal energy E is related to λ by equation 1, which, for a dipole, can be approximated as

$$E \approx (987 \text{ eV})\lambda L^{-8/3} \qquad (38)$$

where λ has units of eV $R_E^{2/3}\gamma^{-2/3}$.

In steady state, the lighter curves would describe trajectories of the ions as they drift around the Earth. One can estimate the closeness of the particular ion species to equilibrium by evaluating the distance from the Alfvĕn layer to the ion's inner edge (both plotted in Figures 23-26). Using this criterion, the higher energy ions (Figures 25-26) are fairly close to "equilibrium" by 1300 UT, while the lower-energy ions,

having much slower drift speeds, have not come to equilibrium yet (Figures 23-24). For more detailed discussion see Paper 2, Section II.B. The high energy ions would have formed a complete or nearly complete ring, corresponding to a recovery-time ring current. They did not do this, however,because our numerical procedure does not allow an inner edge to cross local noon twice (section V.E).

B. General Comments

The results shown in this and the following two papers represent a "first try" at a substorm simulation. This is also our first real confrontation with data, and, as a result, we have gained useful experience from the comparison. We thus can point to some improvements in our model inputs necessary to achieve better agreement with data, such as better time dependent conductivity and magnetic field models, improved time-dependent boundary potentials, inclusion of a pre-existing ring current, a more realistic plasma-sheet energy spectrum, and an improved formula for electron precipitation. Abundant data are also necessary in future simulations in order to improve our input parameters.

General improvements in the model should include better numerical treatment of the region near local noon, the effects of neutral winds, field-aligned potential drops, and allowing the system to come to a more relaxed state before the beginning of the growth phase.

We believe that despite its limitations, our model gives a great deal of insight into magnetospheric dynamics, and we are encouraged by the level of agreement between model predictions and observations.

The following paper (paper 2) presents detailed comparisons with data for the region $L \geq 6$. Paper 3 deals with the electric fields at lower L-values and the resulting motion of the plasmapause.

ACKNOWLEDGEMENTS

We are grateful to H. K. Hills and L. Wald for their help in displaying model results; to D. A. Hardy for his helping to provide data from the S3-2 satellite; to R. D. Sharp and E. Shelley for providing S3-3 particle data; and to A. J. Dessler, D. J. Southwood, and L. R. Lyons for illuminating discussions. This work has been supported in part by the Atmospheric Sciences Section of the National Science Foundation under Grant ATM74-21185, by the U.S. Air Force Geophysics Laboratory under grant F19628-77-C-0005 and by the National Aeronautics and Space Administration under grant NGR44-006-137.

REFERENCES

Atkinson, G., On tail current ions, J. Geophys. Res., 72, 5373, 1967.

Axford, W. I., and C. O. Hines, A unifying theory of high-latitude geophysical phenomena and geomagnetic storms, Can. J. Phys., 39, 1433, 1961.

Axford, W. I., Magnetospheric convection, Rev. Geophys., 7, 421, 1969.

Block, L. P., On the distribution of electric fields in the magnetosphere, J. Geophys. Res., 71, 855, 1966.

Burke, W. J., D. A. Hardy, F. J. Rich, M. C. Kelley, M. Smiddy, B. Schuman, R. C. Sagalyn, R. P. Vancour, P. J. L. Wildman, S. T. Lai, and J. Bass, A case study of S3-2 observations in the late evening auroral oval, Report AFGL-7R-79-0011, U. S. Air Force Geophysics Laboratory, Hanscom AFB MA, 1979.

Burrows, J. R., M. D. Wilson, and I. B. McDiarmid, Simultaneous field aligned current and charged particle measurements in the cleft, in Magnetospheric Particles and Fields, ed. by B. M. McCormac, p. 111, D. Reidel, Hingham, Mass., 1976.

Cole, K. D., On solar-wind generation of polar geomagnetic disturbance, Geophys. J., 6, 103, 1961.

Cowley, S. W. H., Energy transport and diffusion, in Physics of Solar Planetary Environments, ed. D. J. Williams, p. 582, Amer. Geophys. Un., Washington, D.C., 1976.

DeForest, S. E., and C. E. McIlwain, Plasma clouds in the magnetosphere, J. Geophys. Res., 76, 3587, 1971.

Dungey, J. W., Interplanetary magnetic field and the auroral zones, Phys. Rev. Letters, 6, 47, 1961.

Ejiri, M., R. A. Hoffman and P. H. Smith, Energetic particle penetrations into the inner magnetosphere, Goddard Space Flight Center Report X-625-77-254, 1977.

Ejiri, M., R. A. Hoffman and P. H. Smith, The convection electric field model for the magnetosphere based on Explorer 45 observations, J. Geophys. Res. 83, 4911, 1978.

Fejer, J. A., Theory of geomagnetic daily disturbance variations, J. Geophys. Res., 69. 123, 1964.

Feldstein, Y. I., Auroral oval, J. Geophys. Res., 78, 1210, 1973.

Ghielmetti, A. G., R. G. Johnson, R. D. Sharp, and E. G. Shelley, The latitudinal, diurnal, and altitudinal distributions of upward flowing energetic ions of ionospheric origin, Geophys. Res. Lett., 5, 59, 1978.

Gurnett, D. A., Electric field and plasma observations in the magnetosphere, in Critical Problems of Magnetospheric Physics, ed. by E. R. Dyer, p. 123, Inter-Union Commission on Solar-Terrestrial Physics, National Academy of Sciences, Washington, D.C., 1972.

Gizler, V. A., V. S. Semenov, and O. A. Troshichev, Electric fields and currents in the ionosphere generated by field-aligned currents observed by Triad, Planet. Space Sci., 27, 223, 1979.

Harel, M., and R. A. Wolf, Convection, in Physics of Solar-Planetary Environments, Vol. II, ed. by D. J. Williams, p. 617, Amer. Geophys. Un., Washington, D. C., 1976.

Harel, M., R. A. Wolf, and P. H. Reiff, Computer modeling of events in the inner magnetosphere, in Quantitative Modeling of the Magnetospheric Processes, Geophys. Monogr. Ser., Vol. 21, ed. by W. P. Olson, p. 499, AGU, Washington, D. C., 1979.

Harel, M. R. A. Wolf, R. W. Spiro, P. H. Reiff, C.-K. Chen, W. J. Burke, F. J. Rich, and M. Smiddy, Quantitative simulation of a magnetospheric substorm, 2. Comparison with observations, submitted to J. Geophys. Res.,

Harper, R. M., A comparison of ionospheric currents, magnetic variations and electric fields at Arecibo, J. Geophys. Res., 82, 3233, 1977.

Harper, R. M., J. C. G. Walker, Comparison of electrical conductivities in the E-and F-regions of the nocturnal ionosphere, Planet. Space Sci., 25, 197, 1977.

Heelis, R. A., R. W. Spiro, W. B. Hanson, and J. L. Burch, Magnetosphere-ionosphere coupling in the midlatitude trough, EOS (Trans. Am. Geophys. Un.), 57, 990, 1976.

Heppner, J. P., Electric fields in the magnetosphere, in Critical Problems of Magnetospheric Physics, ed. by E. R. Dyer, p. 107, Inter-Union Commission on Solar-Terrestrial Physics, National Academy of Sciences, Washington, D. C., 1972.

Heppner, J. P., Empirical models of high-latitude electric fields, J. Geophys. Res., 82, 115, 1977.

Jaggi, R. K. and R. A. Wolf, Self-consistent calculation of the motion of a sheet of ions in the magnetosphere, J. Geophy. Res., 78, 2842, 1973.

Jones, K. A., and M. H. Rees, Time-dependent studies of the aurora-I. Ion density and composition, Planet. Space Sci., 21, 537, 1973.

Kamide, Y. and S. Matsushita, Simulation studies of ionospheric electric fields and currents in relation to field-aligned currents. 1. Quiet periods, J. Geophys. Res., 84, 4083, 1979a.

Kamide, Y. and S. Matsushita, Simulation studies of ionospheric electric fields and currents in relation to field-aligned currents. 2. Substorms, J. Geophys, Res., 84, 4099, 1979b.

Karlson, E. T., Streaming of plasma through a magnetic dipole field, Phys. Fluids, 6, 798, 1963.

Kennel, C. F., Consequences of a magnetospheric plasma, Rev. Geophys., 7, 379, 1969.

Kivelson, M. G., Magnetospheric electric fields and their variation with geomagnetic activity, Rev. Geophys. Space Phys., 14, 189, 1976.

Klumpar, D. M., J. R. Burrows, and M. D. Wilson, Simultaneous observations of field-aligned currents and particle fluxes in the post-midnight sector, Geophys. Res. Lett., 3, 395 , 1976.

Konradi, A., C. L. Semar, and T. A. Fritz, Injection boundary dynamics during a geomagnetic storm, J. Geophys. Res., 81, 3851, 1976.

Leboeuf, J. N., T. Tajima, C. F. Kennel and J. M. Dawson, Global simulations of the three-dimensional magnetosphere, UCLA preprint PPG-450, 1980.

Mal'tsev, Yu. P., The effect of ionospheric conductivity on the convection system in the magnetosphere, Geomag. Aeron., 4, 128, 1974.

McDiarmid, I. B., E. E. Budzinski, M. D. Wilson, and J. R. Burrows, Reverse polarity field-aligned currents at high latitudes, J. Geophys. Res., 82, 1513, 1977.

McDiarmid, I. B., J. R. Burrows and M. D. Wilson, Comparison of magnetic field perturbations at high latitudes with charged particles and the IMF, J. Geophys. Res., 83, 681, 1978.

McIlwain, C. E., Substorm injection boundaries, in Magnetospheric Physics, edited by B. M. McCormac, p. 143, D. Reidel, Hingham, Mass., 1974.

McPherron, R. L., C. T. Russell and M. P. Aubry, Satellite studies of magnetospheric substorms on August 15, 1968. 9. Phenomenological model of substorms, J. Geophys. Res., 78, 3131, 1973.

Meng, C.-I., R. H. Holzworth, and S.-I. Akasofu, Auroral circle-delineating the poleward boundary of the quiet auroral belt, J. Geophys. Res., 82, 164, 1977.

Mizera, P. F., and J. F. Fennell, Signature of electric fields from high and low altitude particle distributions, Geophys. Res. Lett., 4, 311, 1977.

Mozer, F. S., On the relationship between the growth and expansion phases of substorms and magnetospheric convection, J. Geophys. Res., 78, 1719, 1973.

Nisbet, J. S., M. J. Miller and L. A. Carpenter, Currents and electric fields in the ionosphere due to field-aligned auroral currents, J. Geophys. Res., 83, 2647, 1978.

Nishida, A., Geomagnetic Diagnosis of the Magnetosphere, Springer-Verlag, New, York, p. 159ff, 1978.

Nopper, R. W., Jr., and R. L. Carvillano, Polar equatorial coupling during magnetically active periods, Geophys. Res. Lett., 5, 699, 1978.

Nopper, R. W., Jr., and R. L. Carovillano, Ionospheric electric fields driven by field-aligned currents, in Quantitative Modeling of the Magnetospheric Processes, Geophys. Monogr. Soc., Vol. 21, ed. by W. P. Olson, p. 557, AGU, Washington, D. C., 1979.

Olson, W. P., and K. A. Pfitzer, A quantitative model of the magnetospheric magnetic field, J. Geophys. Res., 79, 3739, 1974.

Rishbeth, H., and O. K. Garriott, Introduction to Ionospheric Physics Academic Press; New York, 1969.

Roederer, J. G., and E. W. Hones, Jr., Motion of magnetospheric particle clouds in a time-dependent electric field model, J. Geophys. Res., 79, 1432, 1974.

Rowe, J. F., and J. D. Mathews, Low-latitude nighttime E-region conductivities, J. Geophys. Res., 78, 7461, 1973.

Shelley, E. G., R. D. Sharp, and R. G. Johnson, Satellite observations of an ionospheric acceleration mechanism, Geophys. Res. Lett., 3, 654, 1976.

Smith, P. H., H. K. Bewtra and R. A. Hoffman, Motions of charged particles in the magnetosphere under the influence of a time-varying large-scale convection electric field, in Quantitative Modeling of the Magnetospheric Processes, Geophys. Monogr. Ser., vol. 21, edited by W. P. Olson, p. 513, AGU, Washington, D. C., 1979.

Southwood, D. J. and R. A. Wolf, An assessment of the role of precipitation in magnetospheric convection, J. Geophys. Res., 83, 5227, 1978.

Spiro, R. W., M. Harel, R. A. Wolf, and P. H. Reiff, Quantitative simulation of a magnetospheric substorm. 3. Plasmaspheric electric fields and the evolution of the plasmapause, submitted to J. Geophys. Res., 1980.

Stern, D. P., Large-scale electric fields in the earth's magnetosphere, Rev. Geophys. Space Phys., 15, 156, 1977.

Swift, D. W., Possible mechanisms for formation of the ring current belt, J. Geophys. Res., 76, 2276, 1971.

Vasyliunas, V. M., A mathematical model of plasma motions in the magnetosphere, Trans. Am. Geophys. Un., 49, 232, 1968.

Vasyliunas, V. M., Mathematical models of magnetospheric convection and its coupling to the ionosphere, in Particles and Fields in the Magnetosphere, ed. by B. McCormac, p. 60, D. Reidel, Dordrecht-Holland, 1970.

Vasyliunas, V. M., The interrelationship of magnetospheric processes, in Earth's Magnetospheric Processes, ed. by B. McCormac, p. 29, D. Reidel, Dordrecht-Holland, 1972.

Volland, H., Models of global electric fields within the magnetosphere, Ann. Geophys., 31, 154, 1975.

Wolf, R. A., Effects of ionospheric conductivity on convective flow of plasma in the magnetosphere, J. Geophys. Res., 75, 4677, 1970.

Wolf, R. A., Calculations of magnetospheric electric fields, in Magnetospheric Physics, ed. by B. M. McCormac, p. 167, D. Reidel, Dordrecht-Holland, 1974.

Wolf, R. A., and M. Harel, Dynamics of the magnetospheric plasma, in Dynamics of the Magnetosphere, ed. by S. I. Akasofu, p. 143, Reidel, Dordrecht-Holland, 1979.

Yasuhara, F. and S. -I. Akasofu, Field-aligned currents and ionospheric electric fields, J. Geophys. Res., 82, 1279, 1977.

APPENDIX

One purpose of this appendix is to derive the formula

$$\underset{\sim}{v}_{Gce} = \frac{\lambda}{q} \frac{\underset{\sim}{B}_e \times \nabla_e \left[\left(\int ds / B\right)^{-2/3}\right]}{B_e^2} \tag{A.1}$$

for the average gradient/curvature drift velocity of the equatorial crossing point of a particle of charge q, for the case of an isotropic distribution of particles; here λ is an energy invariant defined by equation 1 (section II.A), $\underset{\sim}{B}_e$ = equatorial magnetic field, and ∇_e = 2-dimensional equatorial gradient operator. This formula has been derived by others [e.g., Vasyliunas, 1968; Southwood, private communication], but no derivation has been published, as far as we know. The derivation presented here arose out of conversations with D. J. Southwood and G. M. Erickson.

The second purpose of this appendix is to show that, for particles drifting according to a law of the form (A.1), the energy invariant λ, and the number of particles η per unit magnetic flux are constant along a drift path.

Consider a symmetric magnetospheric magnetic-field configuration, with an equatorial plane that is always normal to the local northward-directed magnetic field. Consider only field lines that go through the earth, where the magnetic field is very strong. Assume that the value of the particle kinetic energy E (gyration and bounce motion) is uniquely determined by the equatorial crossing point of the orbit $\underset{\sim}{x}_e$, and by some other parameters that are constant along a drift path. (In the case of

adiabatic motion these other parameters might be the particle's first two adiabatic invariants.) In the case where a pitch-angle scattering process keeps the distribution function isotropic, but the scattering process involves no appreciable energy transfer, the appropriate invariant is λ, where

$$E(\lambda, \underset{\sim}{x}_e) = \lambda [\Xi(\underset{\sim}{x}_e)]^{-2/3} \tag{A.2}$$

where $\Xi(\underset{\sim}{x}_e)$ represents an effective volume occupied by the particles. We will derive an explicit expression for $\Xi(\underset{\sim}{x}_e)$ later (equation A.10). Equation (A.2) is just the statement that, in adiabatic compression of an ideal monatomic gas, the mean thermal energy is proportional to the 2/3 power of the density.

If the particles are $\underset{\sim}{E} \times \underset{\sim}{B}$ and gradient/curvature drifting in a static magnetic-field configuration of the type described above, and drift velocities are small compared to thermal, then the conservation-of-energy relation can be written

$$(\underset{\sim}{v}_{EBe} + \underset{\sim}{v}_{Gce}) \cdot \nabla_e [qV(\underset{\sim}{x}_e) + E(\lambda, \underset{\sim}{x}_e)] = 0 \tag{A.3}$$

where

$$\underset{\sim}{v}_{EBe} \equiv \frac{1}{B_e^2} (-\nabla_e V) \times \underset{\sim}{B}_e \tag{A.4}$$

is the $\underset{\sim}{E} \times \underset{\sim}{B}$-drift velocity in the equatorial plane, and V = electrostatic potential. Using the fact that $\underset{\sim}{v}_{Gce}$ cannot depend on V, the fact that (A.3) holds for $\nabla_e V$ in an arbitrary direction in the equatorial

plane, and some vector identities, we obtain from (A.3):

$$\underset{\sim}{v}_{Gce} = -(qB_e^2)^{-1} \nabla_e E(\lambda, \underset{\sim}{X}_e) \times \underset{\sim}{B}_e \tag{A.5}$$

Any collection of particles that drifts according to a law of the form

$$\underset{\sim}{v}_e = \frac{\underset{\sim}{E}_e \times \underset{\sim}{B}_e}{B_e^2} + \frac{\nabla_e Y \times \underset{\sim}{B}_e}{B_e^2} \tag{A.6}$$

conserves η, the number of particles per unit magnetic flux. To show this, we write the law of conservation of particles, mapped to the equatorial plane, in the form

$$\frac{\partial(\eta B_e)}{\partial t} + \nabla_e \cdot (\eta B_e \underset{\sim}{v}_e) = 0 \tag{A.7}$$

where ηB_e = particles/area mapped to the equatorial plane, and we have assumed that no particles are lost. We now let $\hat{z}$ = northward unit vector in equatorial plane and use (A.6) to rewrite (A.7) in the form

$$B_e\left(\frac{\partial}{\partial t} + \underset{\sim}{v}_e \cdot \nabla_e\right) \eta + \eta \left\{ \frac{\partial B_e}{\partial t} + \nabla_e \cdot [(\underset{\sim}{E}_e + \nabla_e Y) \times \hat{z}] \right\} = 0 \tag{A.8}$$

or, using vector identities and Faraday's law ($\nabla \times \underset{\sim}{E} = -\partial \underset{\sim}{B}/\partial t$),

$$\left(\frac{\partial}{\partial t} + \underset{\sim}{v}_e \cdot \nabla_e\right) \eta = 0 \tag{A.9}$$

We have shown that the convective derivative of η is equal to zero, which

was one of the purposes of this appendix.

Equation A.9 tells us how the effective volume $\Xi(\underset{\sim}{x}_e)$ changes in this convection. Namely, if a set of particles initially occupied one unit of magnetic flux, they will forever occupy one unit of flux. The volume corresponding to one unit of magnetic flux is thus $\int ds/B$, where the integral covers the entire flux tube, and this is the effective volume in (A.2). Thus the relationship between the kinetic energy E of an individual particle and the energy invariant λ is

$$E = \lambda \left[\int ds/B\right]^{-2/3} \qquad (A.10)$$

Here and elsewhere in the paper, the limits of $\int ds/B$ are assumed to be in the northern and southern ionospheres. Substituting (A.10) in (A.5) yields (A.1), which is the equation we set out to derive.

Table 1. Model assumptions.

A. Characteristics of the model

(1) Region of model = inner magnetosphere and ionosphere; $L \lesssim 10$, invariant latitute ≤ 70 .

(2) Olson-Pfitzer analytic magnetic field model and substorm current loop (not self-consistent).

(3) Time dependent ionospheric conductivity model, including day-night asymmetry and auroral enhancement.

(4) $\nabla \cdot \underset{\sim}{j} = 0$ both in magnetosphere and ionosphere. Self-consistently calculated current system, consisting of horizontal ionospheric currents, magnetospheric ring currents, and Birkeland currents connecting the two.

(5) $\underset{\sim}{E} = -\nabla V$ in ionosphere.

(6) Isotropic distribution of particle pitch angles in the magnetosphere.

(7) Discrete particle energy spectrum. Electron energy $\sim$1-4 keV; ion energy $\sim$500 ev - 60 keV.

(8) Electron loss via strong pitch-angle scattering.

(9) Gradient, curvature and $\underset{\sim}{E} \times \underset{\sim}{B}$ drifts included. Polarization currents excluded.

(10) Time-independent particle input at the high-L boundary of the model. Maxwellian input distributions are assumed with $T_i \gtrsim$ 4.5 keV, $T_e \gtrsim$ 1.5 keV at $L \gtrsim 10$.

B. Not Included in the Model

(1) Field-aligned electric fields.

(2) Ionospheric neutral winds.

(3) Pre-existing ring current. All particles assumed to originate at $L \gtrsim 8$.

(4) Polar-cap phenomena. Solar wind and polar cap phenomena enter model only through boundary conditions.

(5) Equatorial electrojet. Equatorial boundary condition is $j_{\text{north-south}} = 0$ at 21° latitude.

Table 2. Computer-Simulation Runs

Computer Run	Peak Polar-Boundary Potential Drop	Conductivity Model	Induction Electric Field
1	80 kV	minimum smoothing	yes
2	80 kV	greater smoothing	yes
3	80 kV	greater smoothing	no
4	140 kV	greater smoothing	yes

Figure Captions

Figure 1. Corresponding regions in the ionosphere and the equatorial plane; mapping is done via the pre-substorm magnetic-field model. The circle I in the ionosphere represents the assumed polar boundary and maps to curve I in the equatorial plane. Our computer model applies to the region equatorward and earthward of curve I.

Figure 2. Overall logic diagram of our program. Arrows indicate flow of information in the program. Dashed lines indicate features that we plan to incorporate in the program, but are not included yet. The rectangles at the corners of the central pentagon represent basic parameters computed. Input models are indicated by rectangles with round corners; input data are indicated by curly brackets. The program cycles through the entire main loop (including all the rectangular boxes) every time step Δt (approximately every 30 seconds). The basic equations that the computer uses or solves are described briefly by words or symbols next to the logic-flow lines.

Figure 3. Fort Churchill H-magnetogram and polar cap potential drop for 19 September 1976. Top panel shows the negative bay for the event we model (onset at about 1000 GMT, maximum at 1050). The 1050 dip is $\simeq 520\gamma$. A small disturbance is seen around 0600 GMT. Bottom panel gives estimates of polar cap potential drop ($\int \underset{\sim}{E} \cdot \underset{\sim}{dl}$) across the polar cap for various crossings by satellite S3-2. Rectangular boxes represent potential drops

from field reversal to field reversal, the sizes of which gives the uncertainties in the integration. Vertical lines (between 1000 UT and 1200 UT) represent our polar boundary potential drop, where we use the region-1 currents to locate the boundary. The solid line represents our main choice runs (1, 2, and 3 in Table 2.) Dashed curves give an alternative choice with peak potential drop of 140 kV (run 4).

Figure 4. Precipitating electron energy flux, east-west magnetic perturbations, ΔB, and forward component of electric field for orbit 4079A-Southern hemisphere. (S3-2 satellite data). Arrows in bottom panel point to the most equatorward electric field reversal; vertical lines show the equatorward edge of the region-1 currents.

Figure 5. Same as figure 4 except that data from orbit 4079A North is plotted (polar cap crossing of roughly 1050 UT). Also shown on Figure 5 are features of the Lockheed particle detector on the S3-3 satellite at comparable invariant latitudes (nearly simultaneous): the top panel shows features of the electron detector (weak, hot, cool), plus the locations of "inverted V's" (shown by carats). The middle panel shows features of the ion fluxes (weak, strong), plus the locations of upward flowing ions (indicated by "UFI").

Figure 6. Same as Figure 4. South pole crossing occurring at about 1140 UT.

Figure 7. Schematic diagram of the substorm current loop. View is from above the equatorial plane. Arrows indicate direction of the

current. Loop includes an equatorial segment (eastward current in the tail), a westward electrojet in the polar ionosphere and two segments of field aligned currents.

Figure 8. Contours of constant magnetic field in the equatorial plane. View is from above the north magnetic pole. Spacing between successive contours follows a logarithmic scale. Values (in Gammas) are given for a few contours.

Figure 9. Pedersen and Hall conductivity profiles for various latitudes in the ionosphere. Height integrated conductivity in mhos is plotted vs. local time for constant invariant latitudes of 55°, 60°, 65° and 70°; and constant universal time of 1150 (peak polar-cap potential drop). Tic marks are spaced 2 mhos apart. The values correspond to run 1, which features the least smoothing at the plasma's low-latitude edge of the auroral zone.

Figure 10. Auroral conductivity profiles for various times during the substorm. Plot format is the same as Figure 9. Latitude is the same for all profiles (70° = poleward region of the auroral oval). Conductivity profiles are given, starting from the top panel, for 0900 (beginning of growth phase), 1000 + ε (onset), 1050 (peak of substorm), 1150 and 1300 (at which we terminated our runs).

Figure 11. Initial potential distribution and plasma "inner edge" locations, in the equatorial plane. The sun is to the left. Equipotentials are 6 kV apart and plotted in the rest frame of the Earth. Also plotted are "inner edges" of three sample

particles (out of 21 different "energy invariant" species) that we monitor. The inner edge was arbitrarily chosen to be $\approx 10\ R_E$ for this initial configuration (corresponds to 0700 UT).

Figure 12. Potential contours without corotation in the equatorial plane. Potential distribution and locations of the "inner edges" were computed two hours after the initial arbitrary starting condition shown in Fig. 11. The closed solid curve at $L \approx 10$ is the boundary of our calculation.

Figure 13. Equipotential contours in the ionosphere. The view is from above the north pole. The spacing between two successive contours is 6 kV. The inner circle is our assumed boundary curve I and is offset 2° toward midnight. Also plotted are the inner edges of 3 of the 21 types of particles we model.

Figure 14. Same as Figure 12 except for the inclusion of the corotation potential. The saddle point potential (15.4 kV contour) is also plotted.

Figure 15. Same as Figure 12 except for a different time 1000-ε UT (just before onset).

Figure 16. Same as Figures 12 and 15. Equipotentials are plotted for 1000+ε UT, following the conductivity jump at onset.

Figure 17. Same as Figures 12-16. Contours are plotted for 1050 UT (peak of expansion phase).

Figure 18. Contours of electrostatic potentials without corotation in the equatorial plane at 1150 UT (corresponding to peak in cross-polar-cap potential drop). Format is the same as

previous figures.

Figure 19. Same as Figure 17, but for 1300 UT, deep into the recovery phase. All of our simulation runs were terminated at 1300 UT.

Figure 20. Total electric field in the equatorial plane (1300 UT). Arrows give the direction and magnitude of the combined potential and induction field.

Figure 21. Velocity flow field in the equatorial plane. This velocity field is $\underset{\sim}{E} \times \underset{\sim}{B}/B^2$ drift velocity where $\underset{\sim}{E}$ is the electric field of Figure 19. Arrows give the instantaneous velocity vector of cold plasma particles.

Figure 22. Total flow field in the ionosphere for 1300 UT. Noon is upward. Circles representing constant latitude are spaced 10° apart.

Figure 23. Instantaneous trajectories and inner edges (dashed curves) for ions with $\lambda = 478 \text{ eV } R_E^{2/3} \gamma^{-2/3}$. The Alfvén-layer and the inner edge curves, for a given time, are darker than the other trajectories. The plots are equatorial-plane views for various phases of the substorm.

Figure 24. Same as Figure 23, but for $\lambda = 1730 \text{ eV } R_E^{2/3} \gamma^{-2/3}$

Figure 25. Same as Figures 23-24, but for $\lambda = 3880 \text{ eV } R_E^{2/3} \gamma^{-2/3}$

Figure 26. Same as Figures 23-25, but for $\gamma = 8650 \text{ eV } R_E^{2/3} \gamma^{-2/3}$

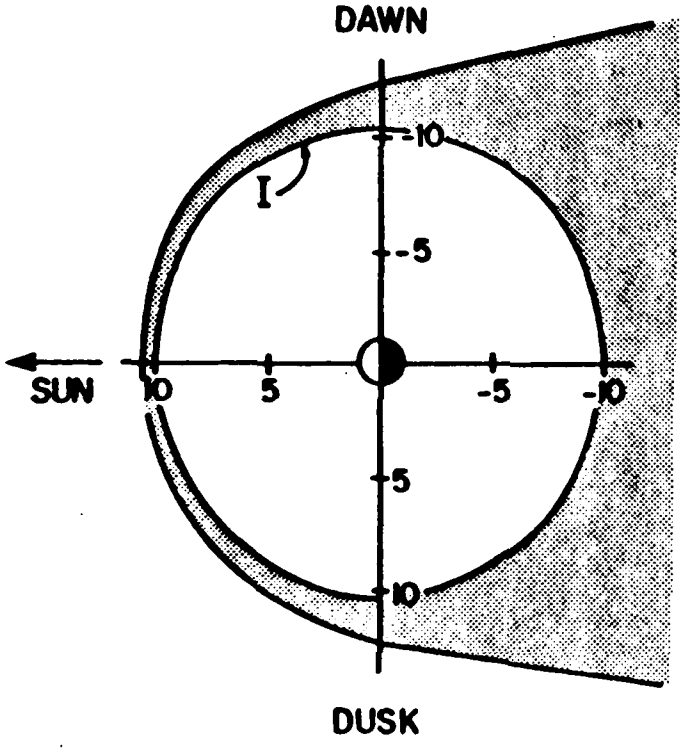

EQUATORIAL PLANE

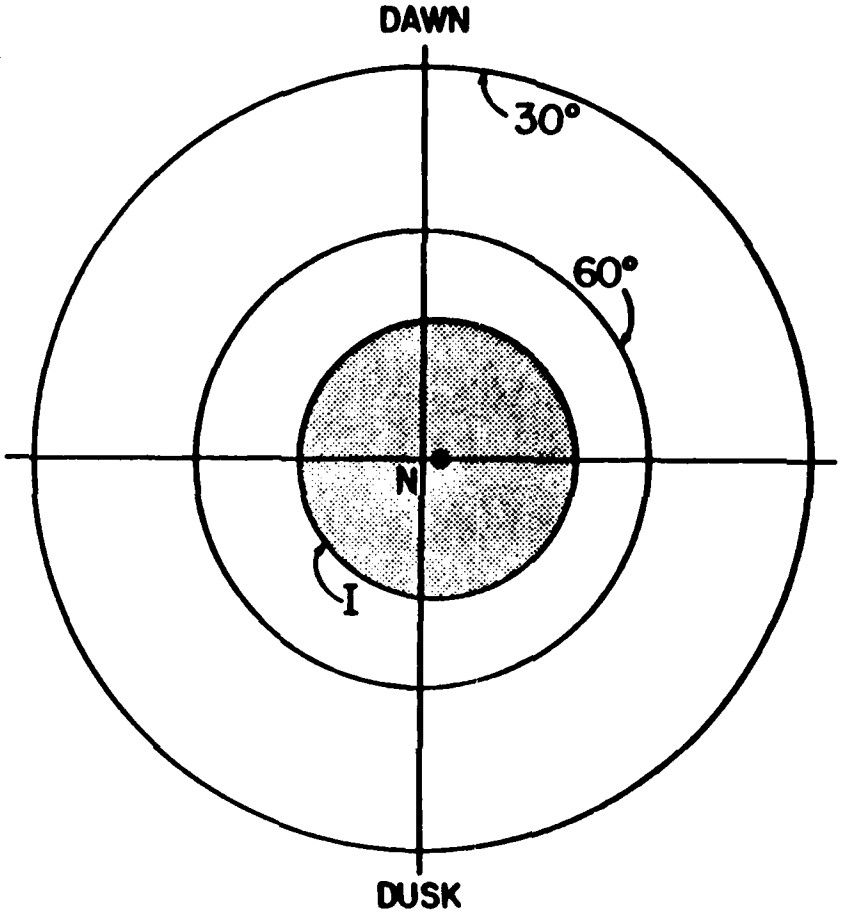

IONOSPHERE

Figure 1

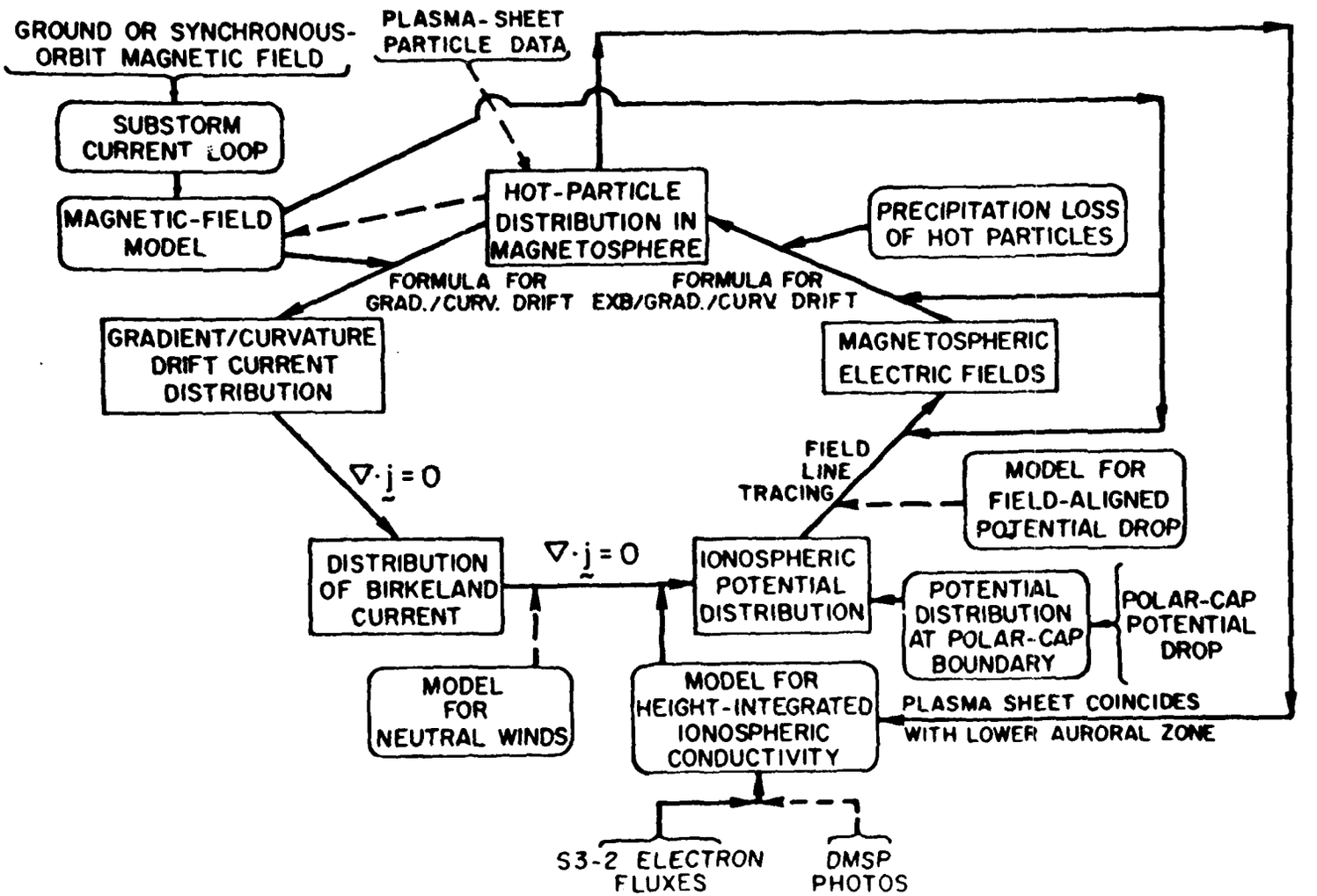
GROUND OR SYNCHRONOUS-ORBIT MAGNETIC FIELD
PLASMA-SHEET PARTICLE DATA
SUBSTORM CURRENT LOOP
MAGNETIC-FIELD MODEL
HOT-PARTICLE DISTRIBUTION IN MAGNETOSPHERE
PRECIPITATION LOSS OF HOT PARTICLES
FORMULA FOR GRAD./CURV. DRIFT
FORMULA FOR EXB/GRAD./CURV. DRIFT
GRADIENT/CURVATURE DRIFT CURRENT DISTRIBUTION
MAGNETOSPHERIC ELECTRIC FIELDS
$\nabla \cdot \underset{\sim}{j} = 0$
FIELD LINE TRACING
MODEL FOR FIELD-ALIGNED POTENTIAL DROP
DISTRIBUTION OF BIRKELAND CURRENT
$\nabla \cdot \underset{\sim}{j} = 0$
IONOSPHERIC POTENTIAL DISTRIBUTION
POTENTIAL DISTRIBUTION AT POLAR-CAP BOUNDARY
POLAR-CAP POTENTIAL DROP
MODEL FOR NEUTRAL WINDS
MODEL FOR HEIGHT-INTEGRATED IONOSPHERIC CONDUCTIVITY
PLASMA SHEET COINCIDES WITH LOWER AURORAL ZONE
S3-2 ELECTRON FLUXES
DMSP PHOTOS

Figure 2

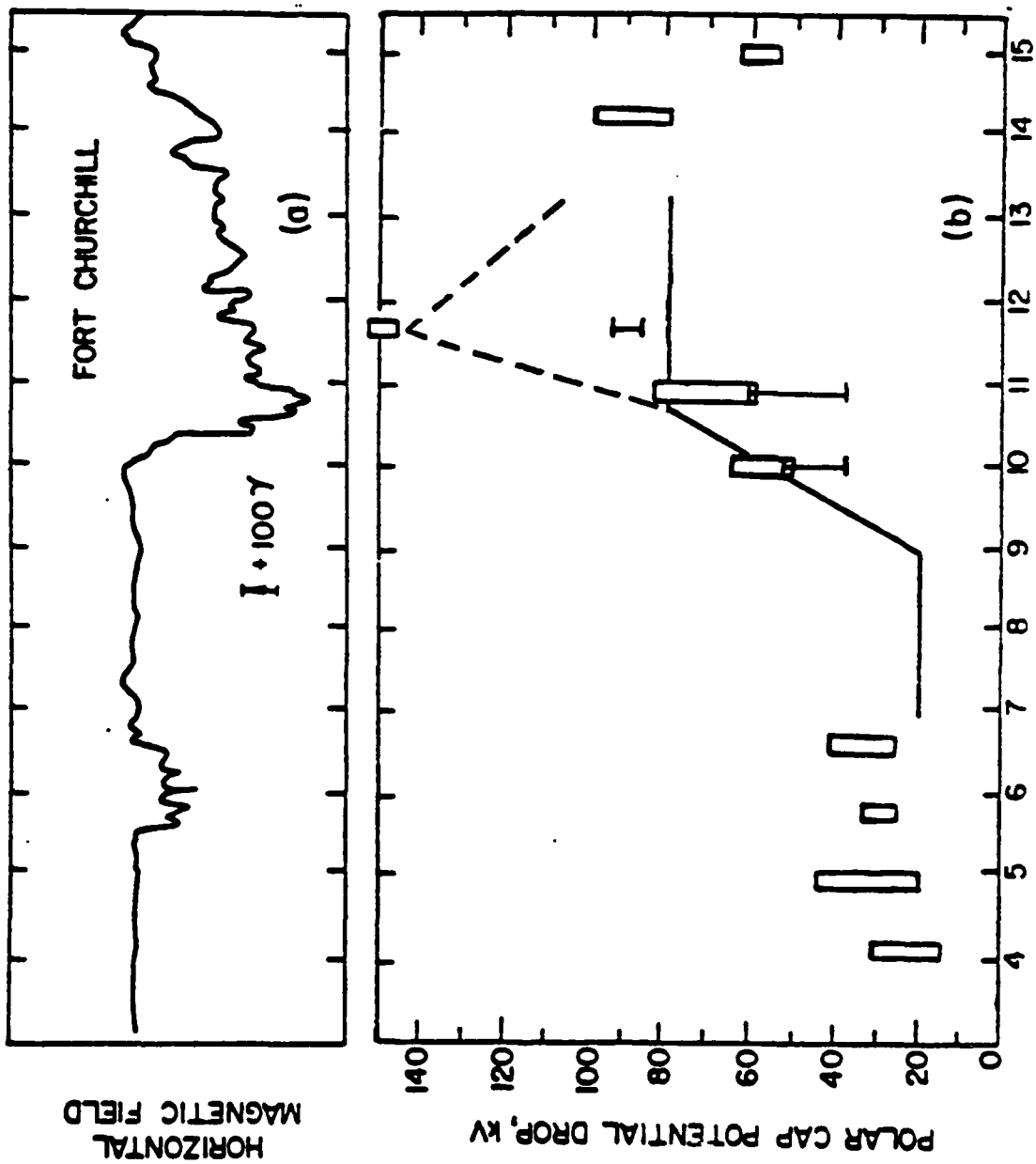
FORT CHURCHILL
(a)
100γ
HORIZONTAL MAGNETIC FIELD
(b)
POLAR CAP POTENTIAL DROP, kV
0
20
40
60
80
100
120
140
4
5
6
7
8
9
10
11
12
13
14
15
UT

Figure 3

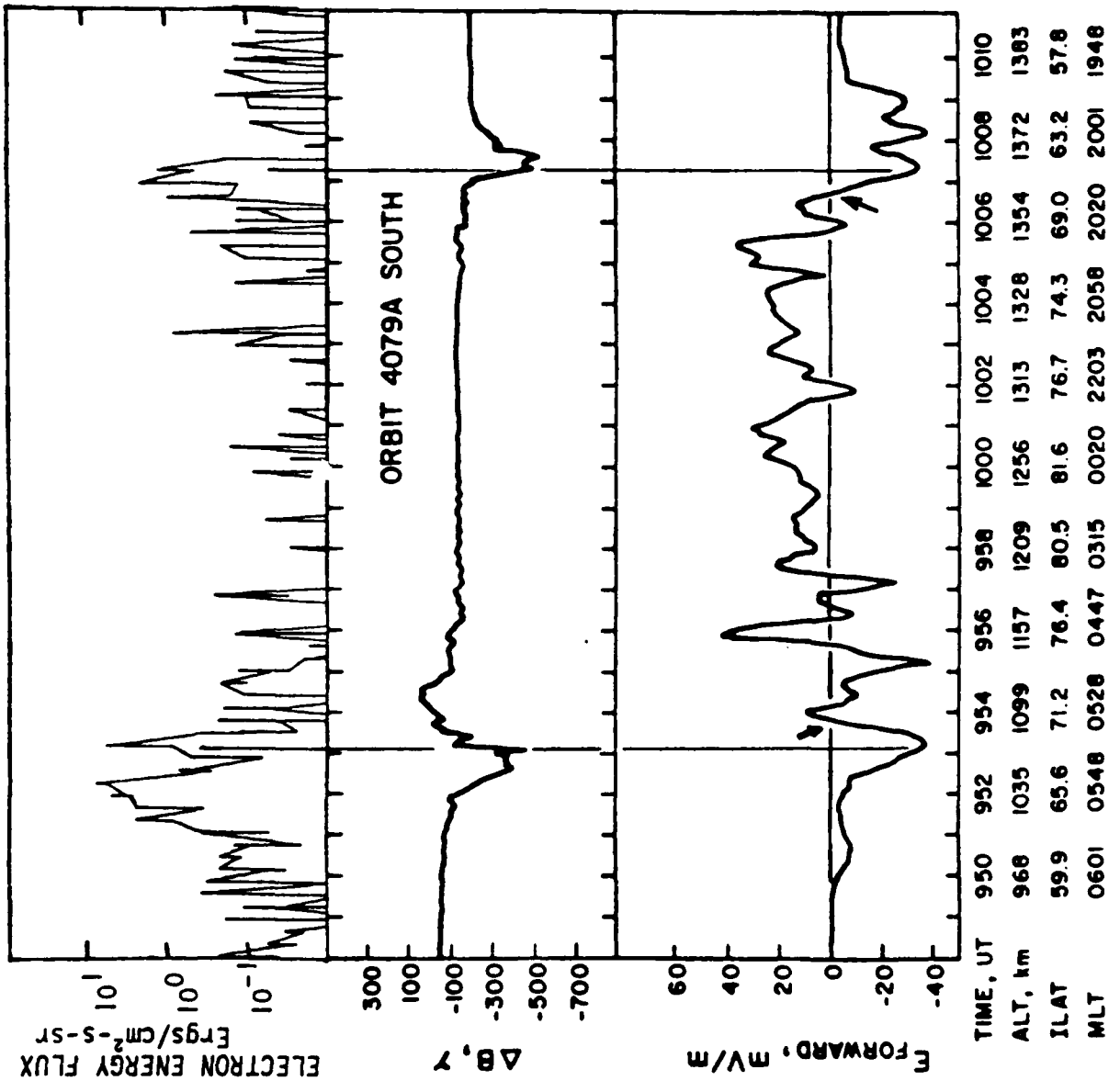
ELECTRON ENERGY FLUX
Ergs/cm²-s-sr
10⁻¹
10⁰
10¹
ΔB, γ
300
100
-100
-300
-500
-700
ORBIT 4079A SOUTH
E FORWARD, mV/m
60
40
20
0
-20
-40
TIME, UT 950 952 954 956 958 1000 1002 1004 1006 1008 1010
ALT, km 968 1035 1099 1157 1209 1256 1313 1328 1354 1372 1383
ILAT 59.9 65.6 71.2 76.4 80.5 81.6 76.7 74.3 69.0 63.2 57.8
MLT 0601 0548 0528 0447 0315 0020 2203 2058 2020 2001 1948

Figure 4

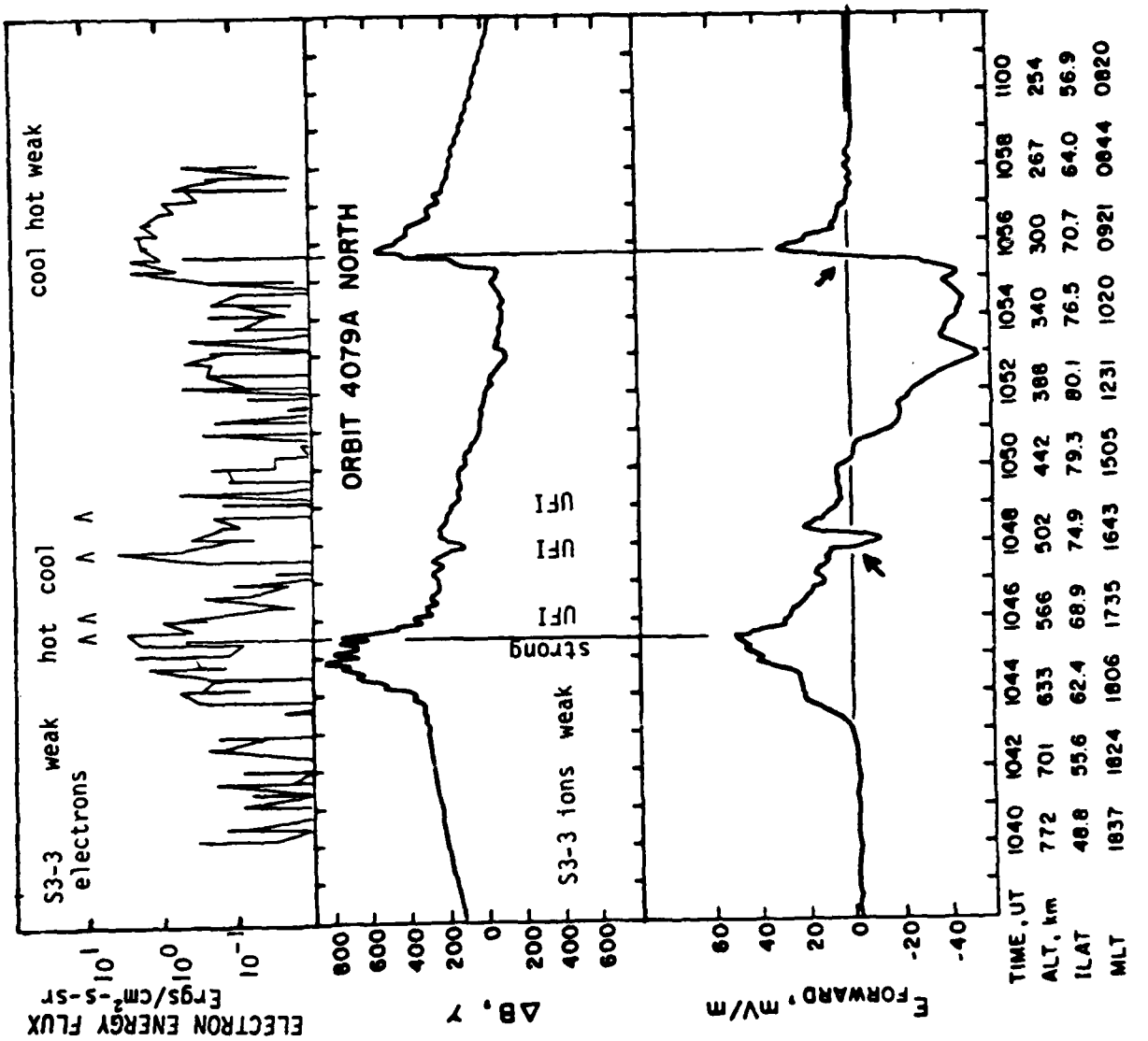
S3-3 electrons
weak hot cool
cool hot weak
ELECTRON ENERGY FLUX
ergs/cm²-s-sr
ORBIT 4079A NORTH
ΔB, γ
S3-3 ions weak
strong
UFI
UFI
UFI
E FORWARD, mV/m
TIME, UT 1040 1042 1044 1046 1048 1050 1052 1054 1056 1058 1100
ALT, km 772 701 633 566 502 442 388 340 300 267 254
ILAT 48.8 55.6 62.4 68.9 74.9 79.3 80.1 76.5 70.7 64.0 56.9
MLT 1837 1824 1806 1735 1643 1505 1231 1020 0921 0844 0820

Figure 5

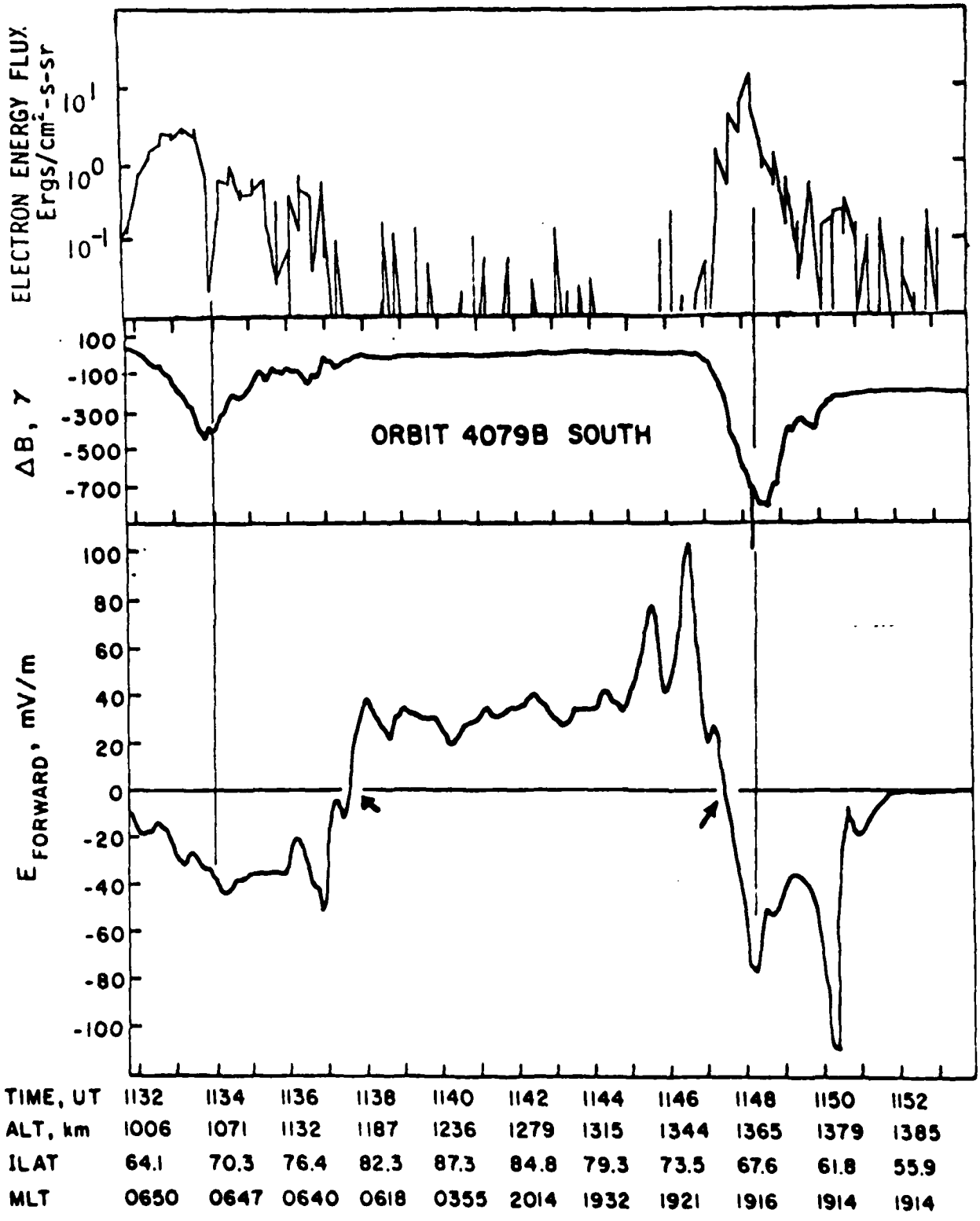
ELECTRON ENERGY FLUX
Ergs/cm²-s-sr
10¹
10⁰
10⁻¹
ΔB, γ
100
-100
-300
-500
-700
ORBIT 4079B SOUTH
E FORWARD, mV/m
100
80
60
40
20
0
-20
-40
-60
-80
-100
TIME, UT 1132 1134 1136 1138 1140 1142 1144 1146 1148 1150 1152
ALT, km 1006 1071 1132 1187 1236 1279 1315 1344 1365 1379 1385
ILAT 64.1 70.3 76.4 82.3 87.3 84.8 79.3 73.5 67.6 61.8 55.9
MLT 0650 0647 0640 0618 0355 2014 1932 1921 1916 1914 1914

Figure 6

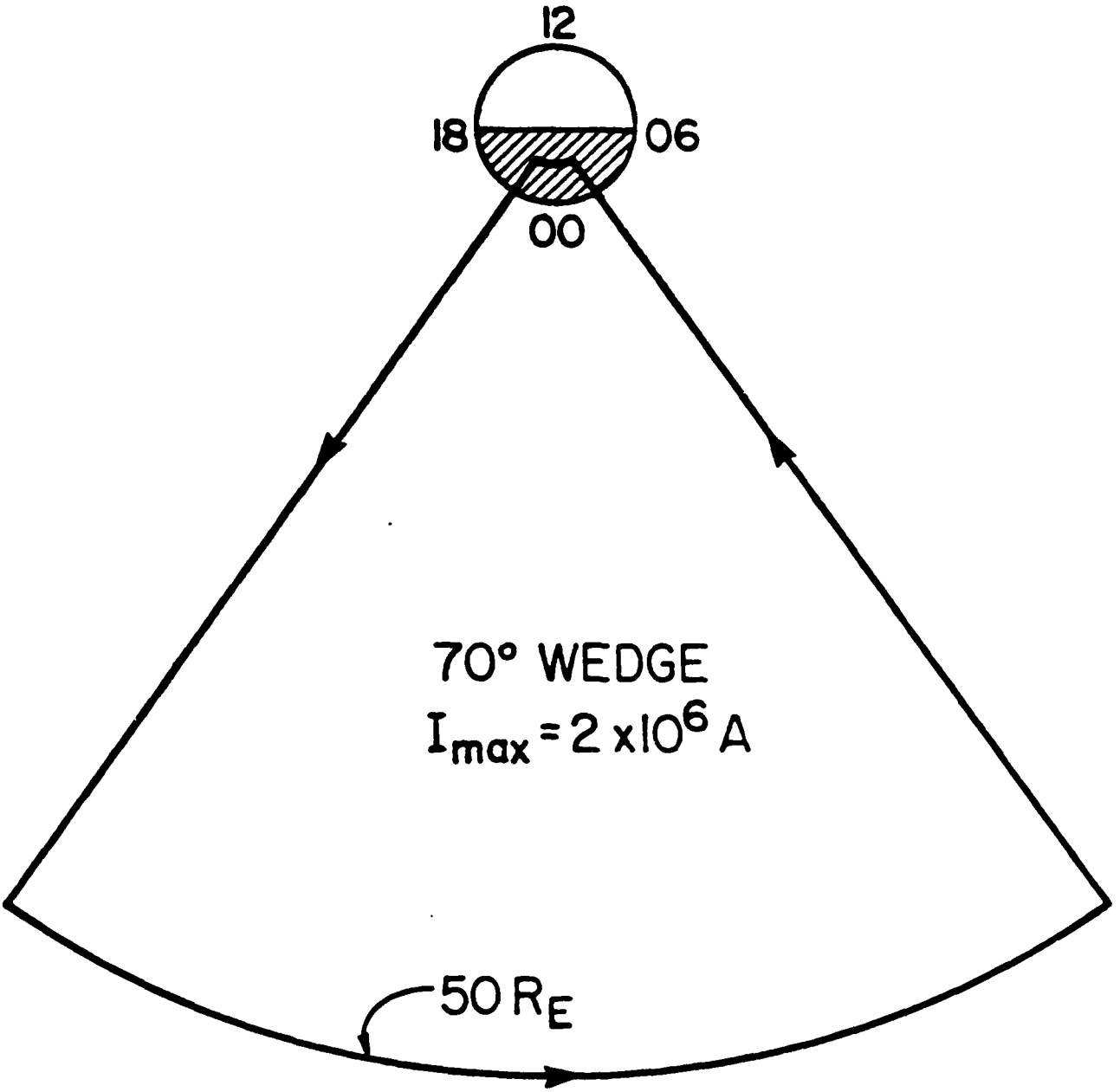

Figure 7

CASE 2 CONTOURS OF CONSTANT MAGNETIC FIELD

TIME = 9:00

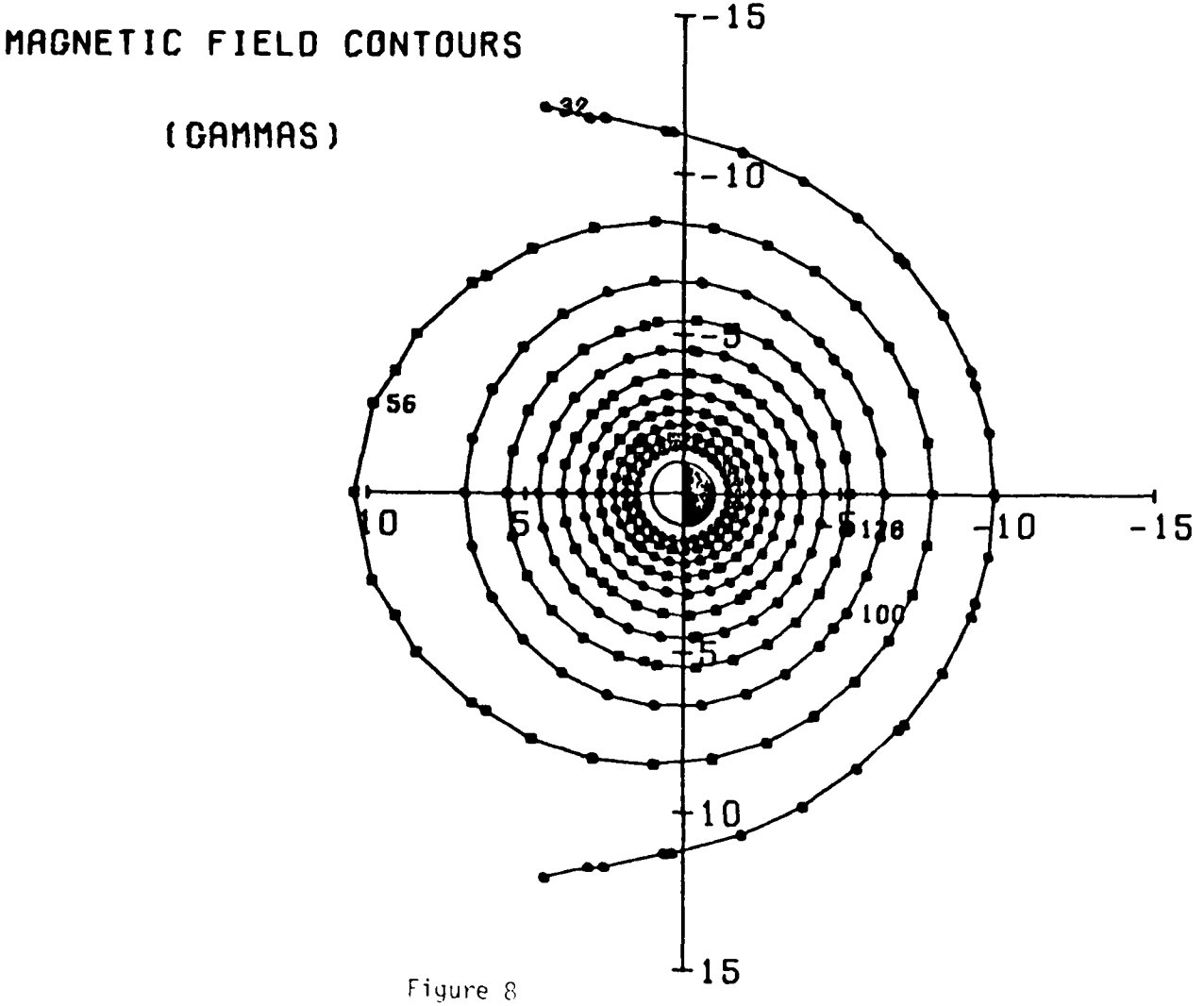

Figure 8

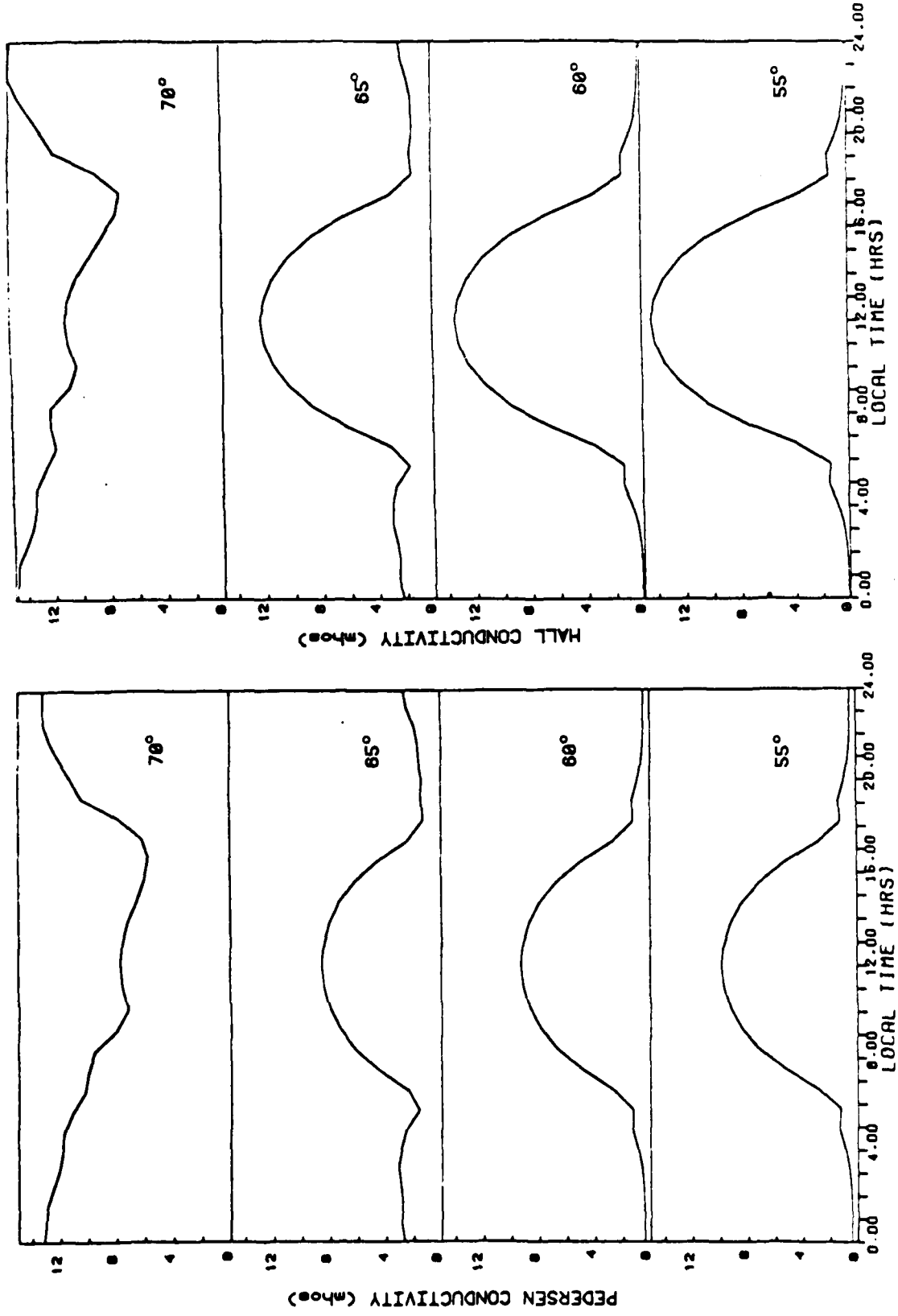
HALL CONDUCTIVITY (mhos)
PEDERSEN CONDUCTIVITY (mhos)
70°
65°
60°
55°
0
4
8
12
0.00
4.00
8.00
12.00
16.00
20.00
24.00
LOCAL TIME (HRS)

Figure 9

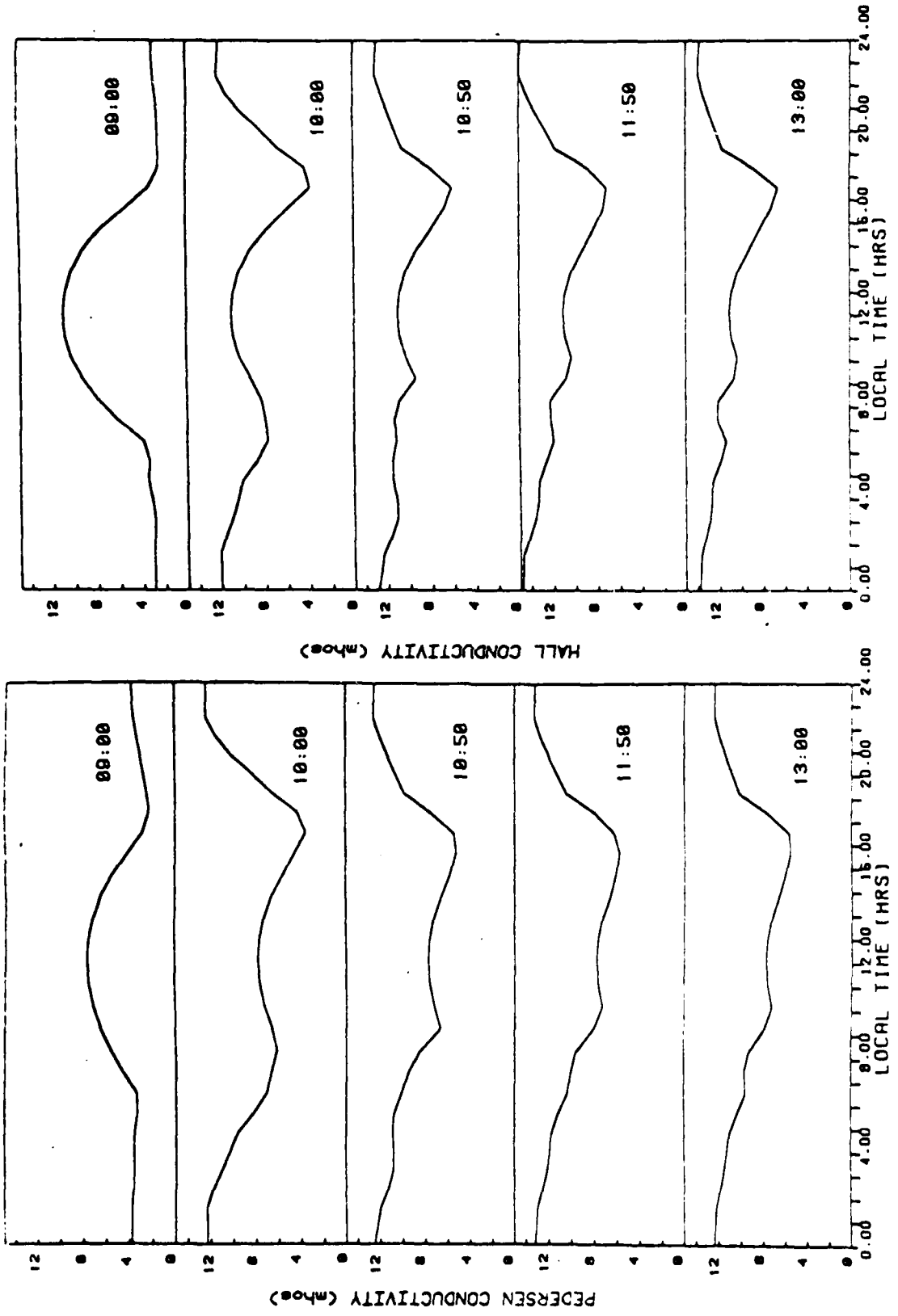
HALL CONDUCTIVITY (mhos)
PEDERSEN CONDUCTIVITY (mhos)
00:00
10:00
10:50
11:50
13:00
0.00
4.00
8.00
12.00
16.00
20.00
24.00
LOCAL TIME (HRS)
12
8
4
0

Figure 10

CASE 1 POTENTIAL CONTOURS W/O COROTATION (KV) K=2.11.21

TIME = 7:00

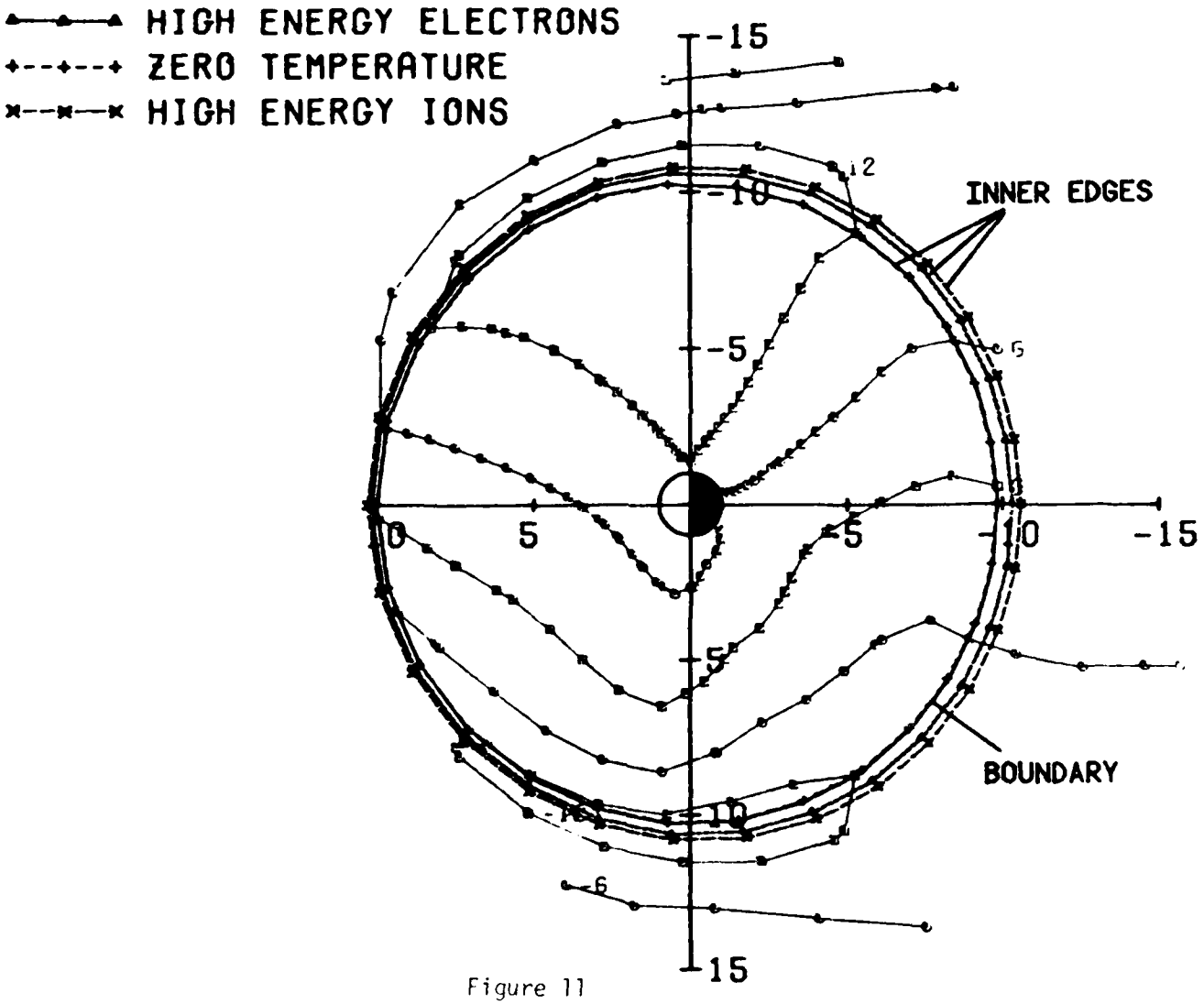

Figure 11

CASE 1 POTENTIAL CONTOURS W/O COROTATION (KV) K=2.11.21

TIME = 9:00

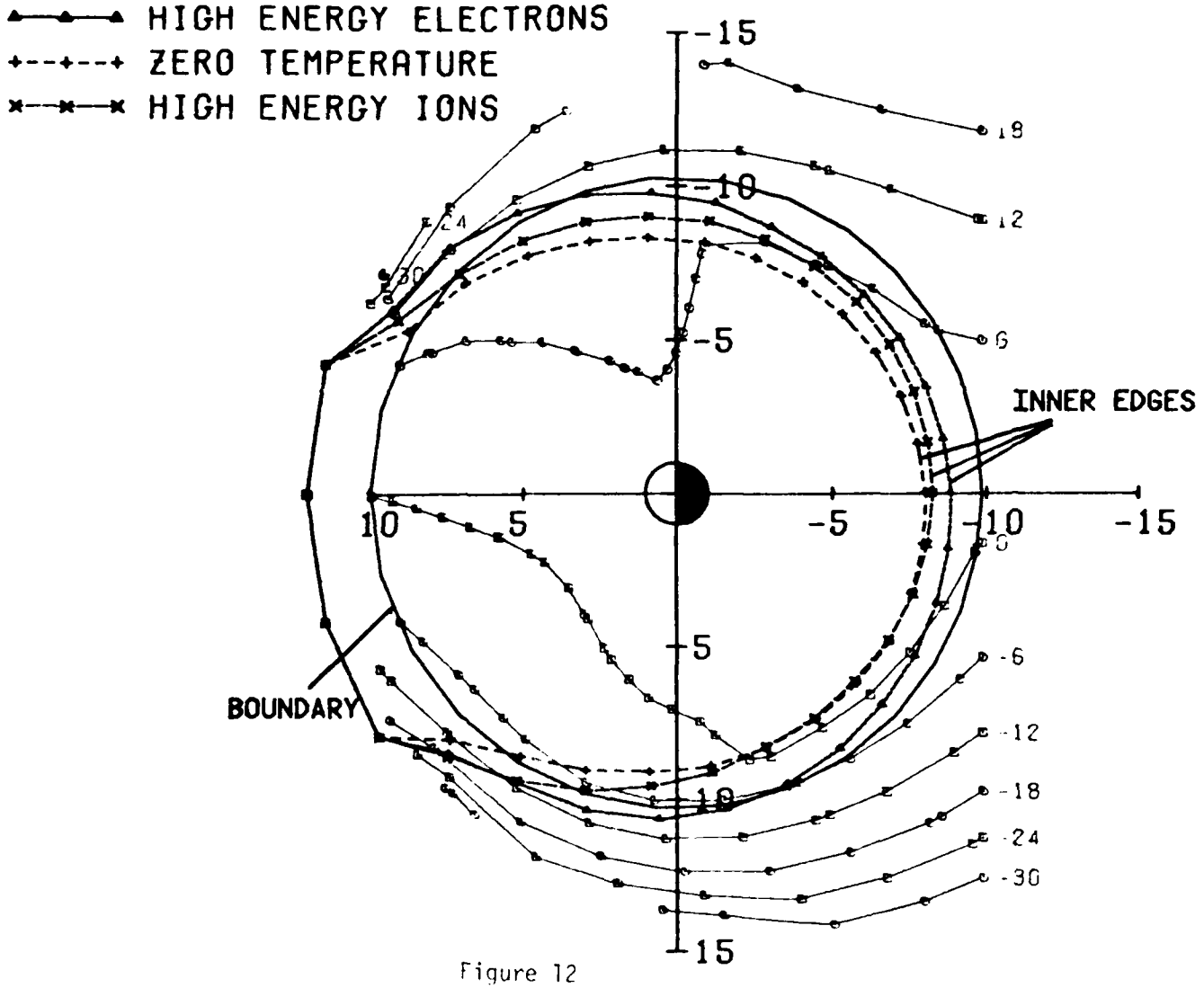

Figure 12

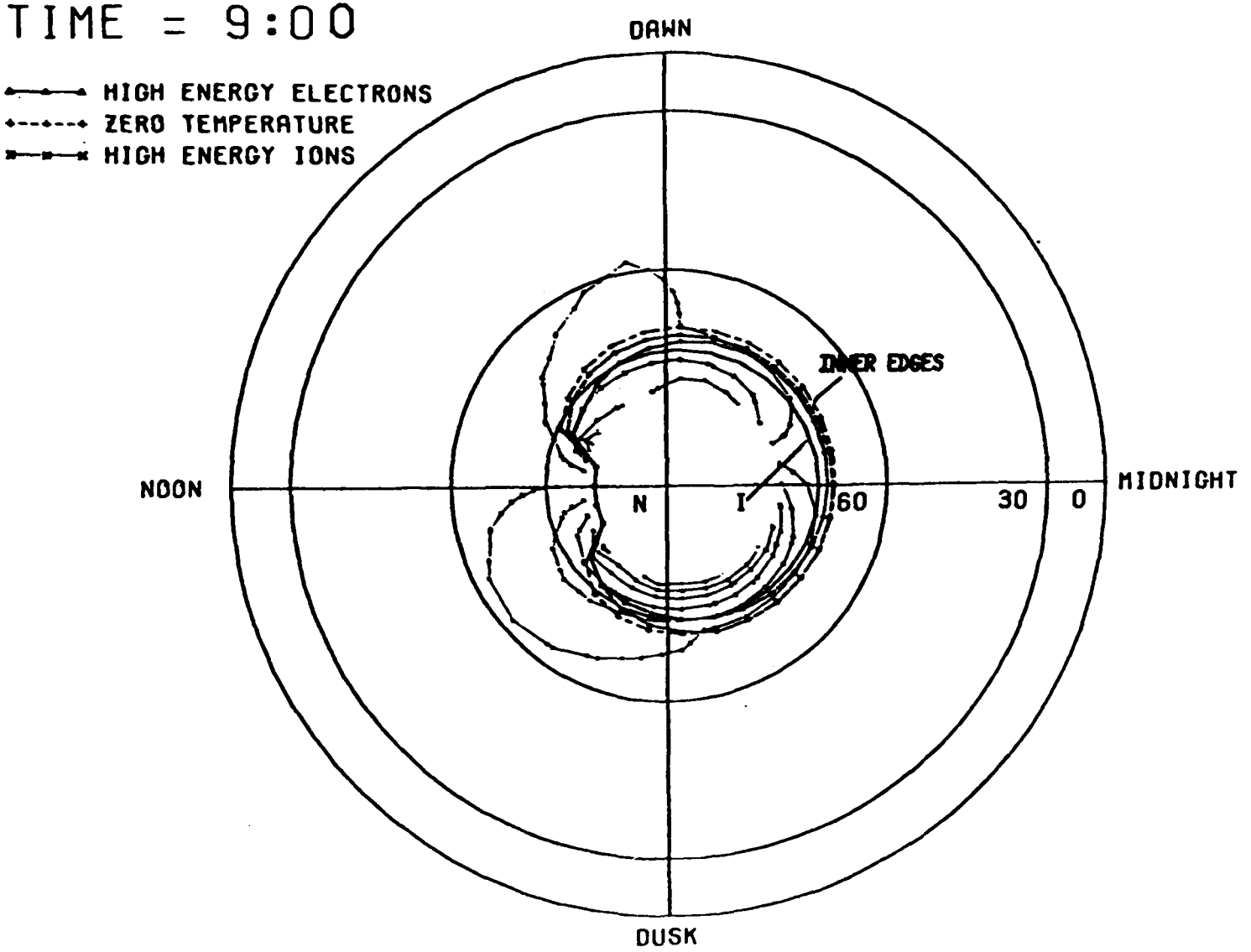
CASE 1 POTENTIAL CONTOURS W/O COROTATION (KV) K=2.11.21 IC=1
TIME = 9:00
HIGH ENERGY ELECTRONS
ZERO TEMPERATURE
HIGH ENERGY IONS
DAWN
NOON
MIDNIGHT
DUSK
INNER EDGES
N
I
60
30
0

Figure 13

CASE 1 POTENTIAL CONTOURS WITH COROTATION (KV) K=2,11,21

TIME = 9:00

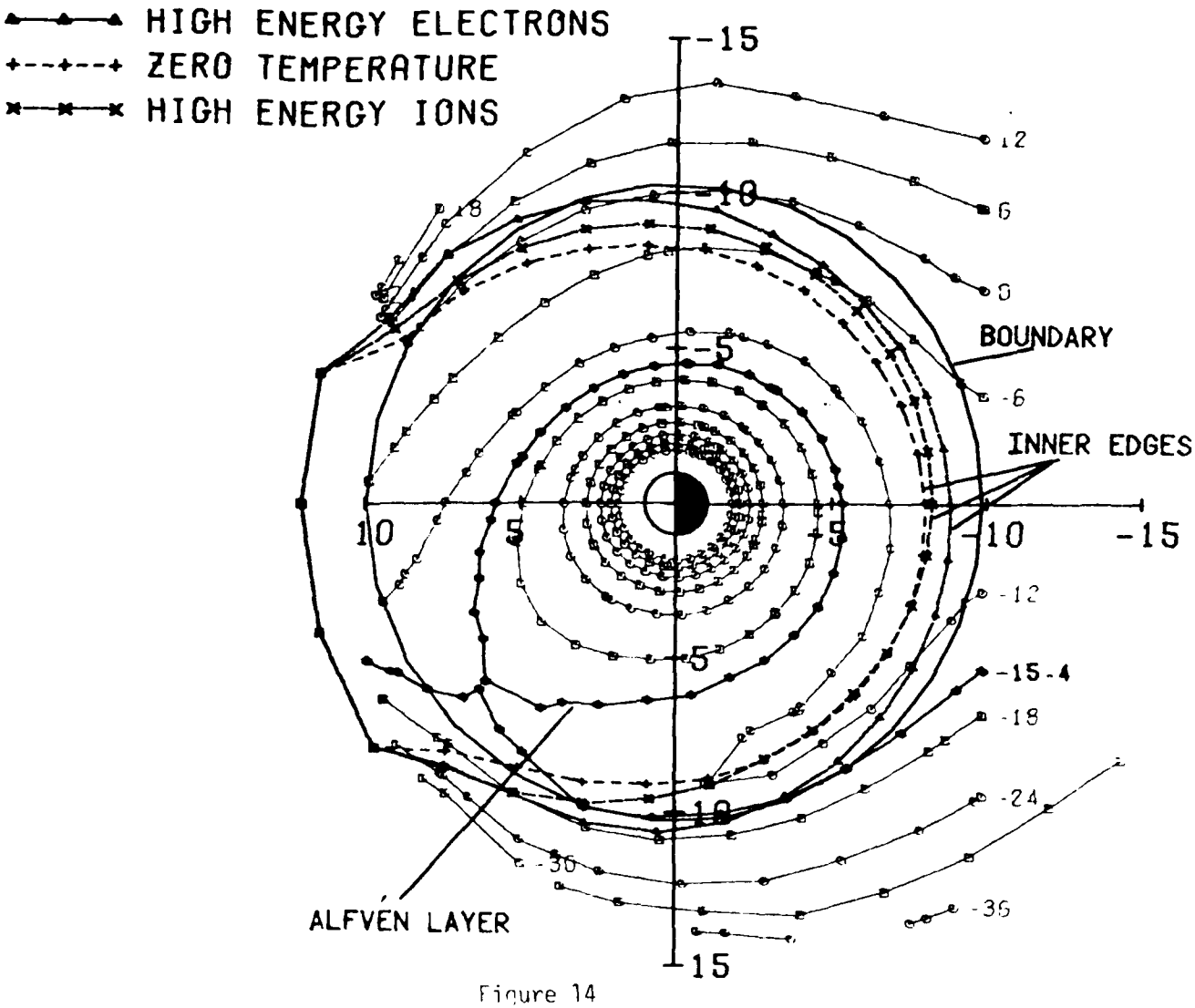

Figure 14

CASE 1 POTENTIAL CONTOURS W/O COROTATION (KV) K=2,11,21

TIME = 10:00-ε

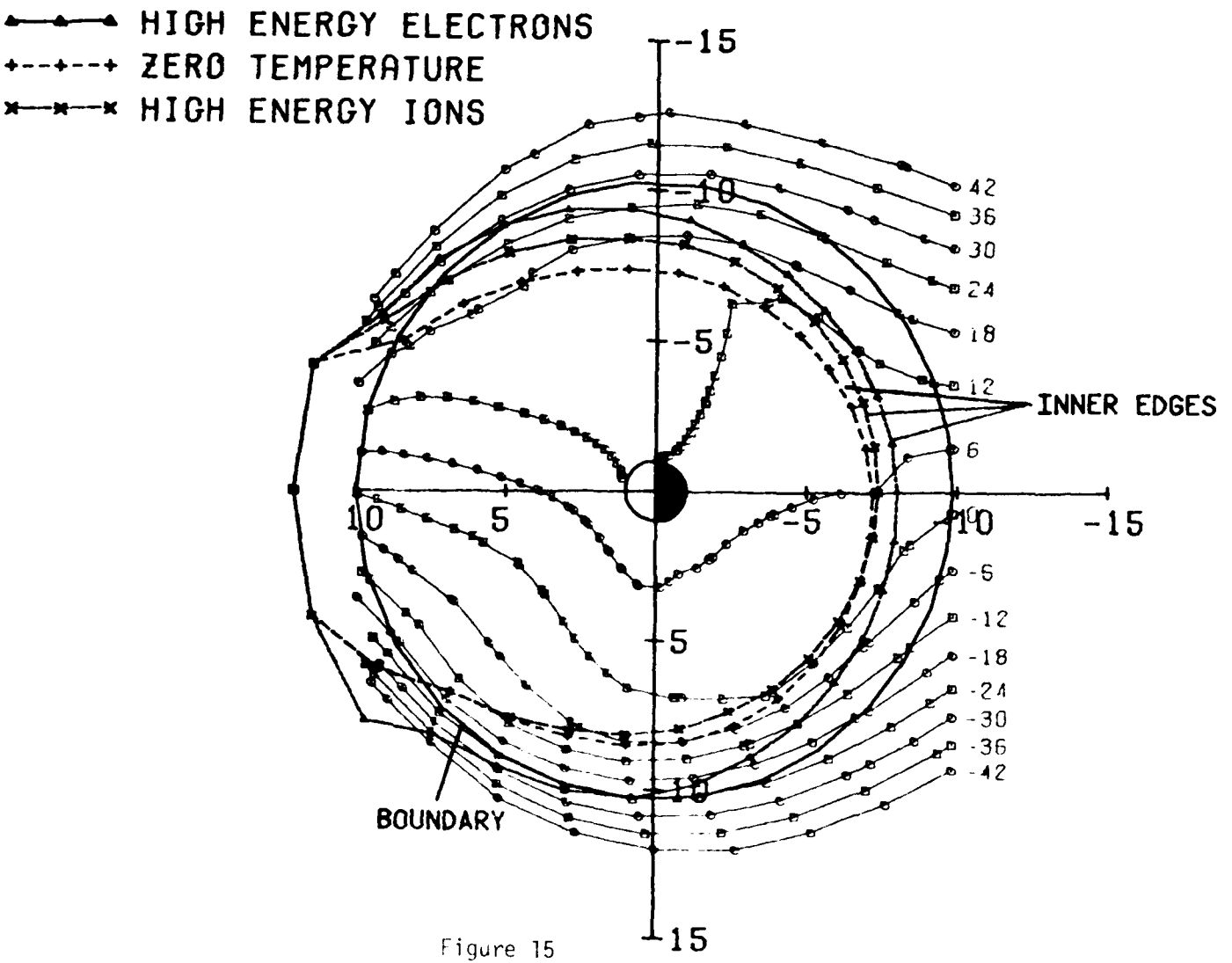

Figure 15

CASE 1 POTENTIAL CONTOURS W/O COROTATION (KV) K=2,11,21

TIME = 10:00+ε

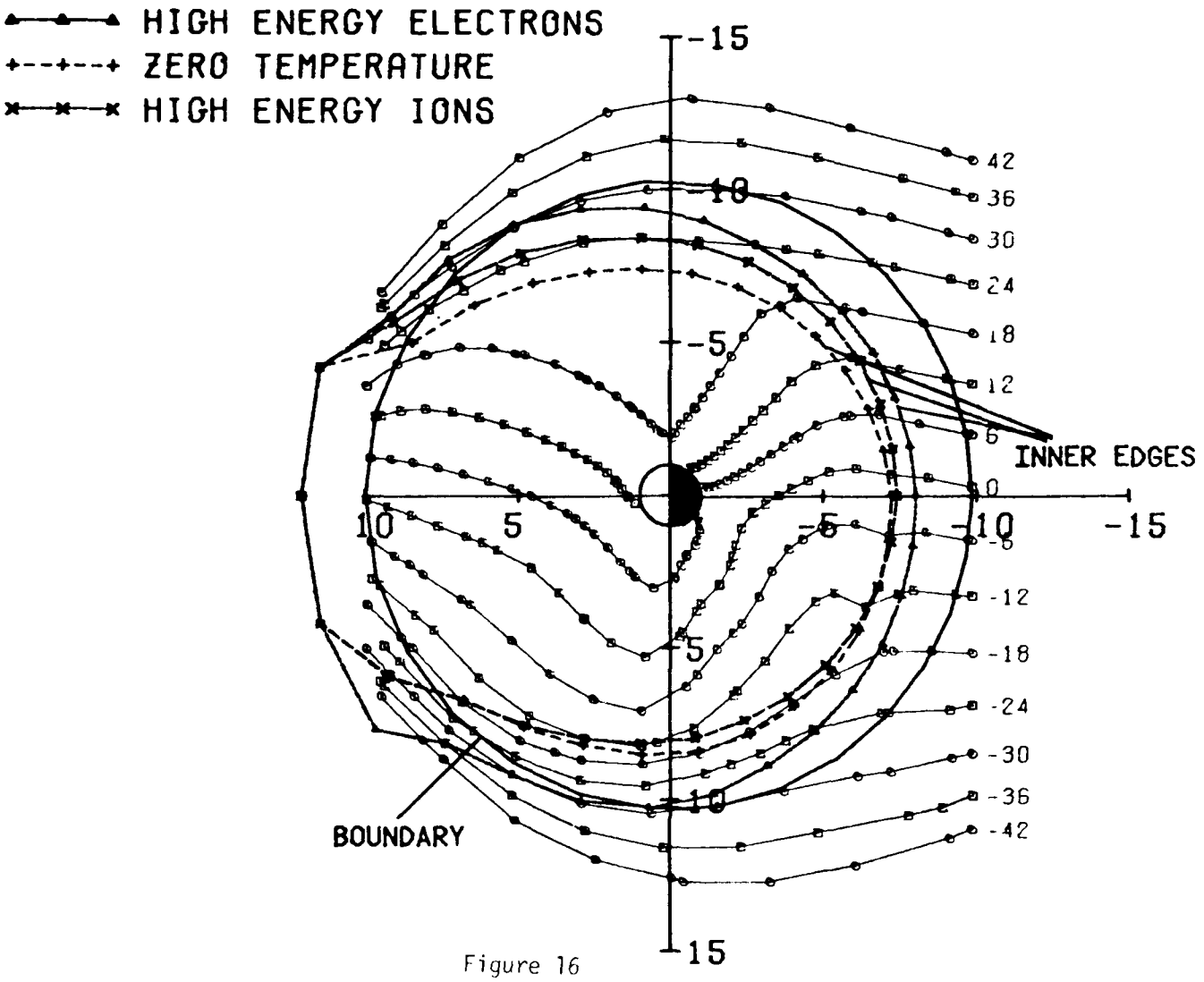

Figure 16

CASE 1 POTENTIAL CONTOURS W/O COROTATION (KV) K=2,11,21

TIME = 10:50

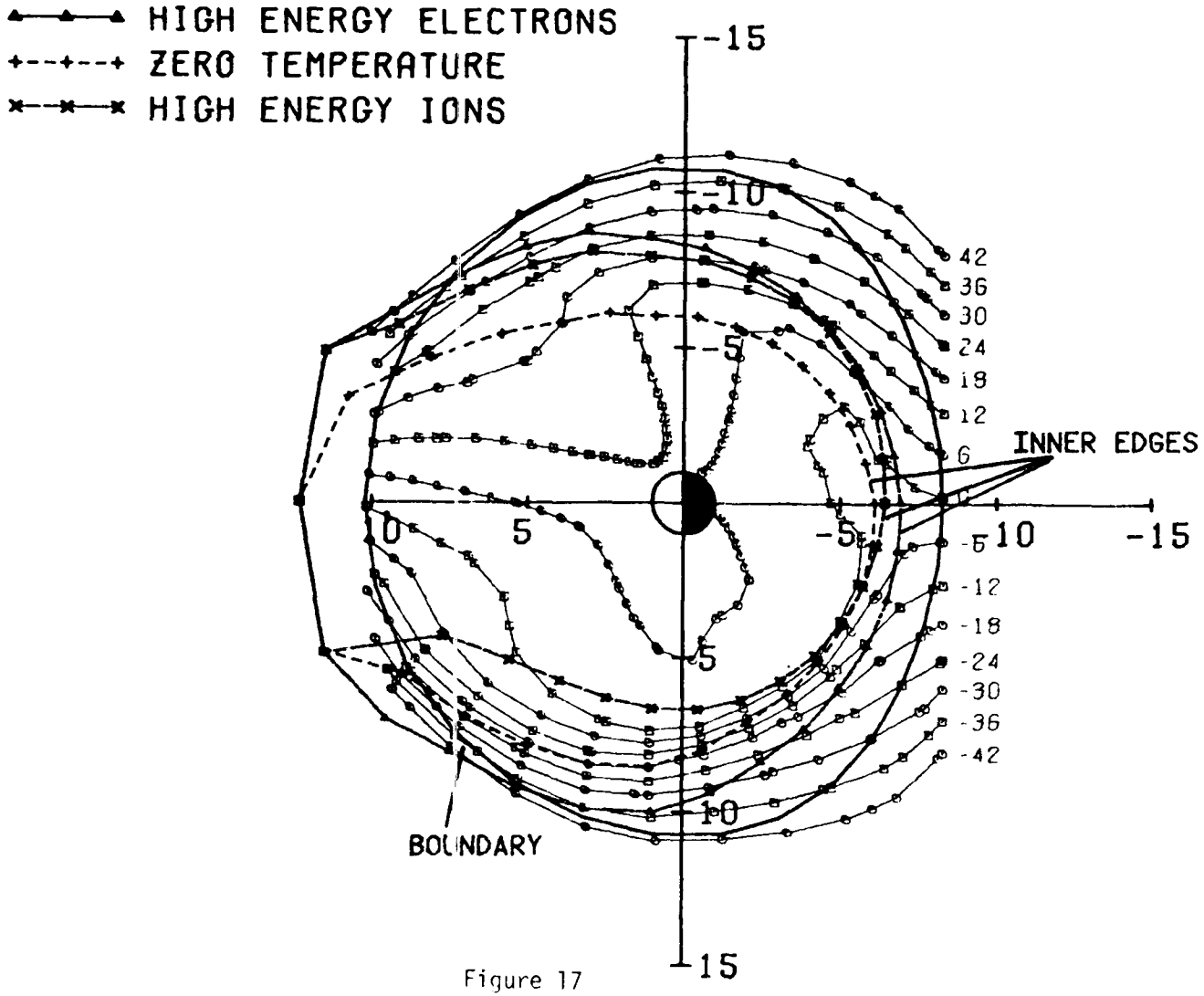

Figure 17

CASE 1 POTENTIAL CONTOURS W/O COROTATION (KV) K=2.11.21

TIME = 11:50

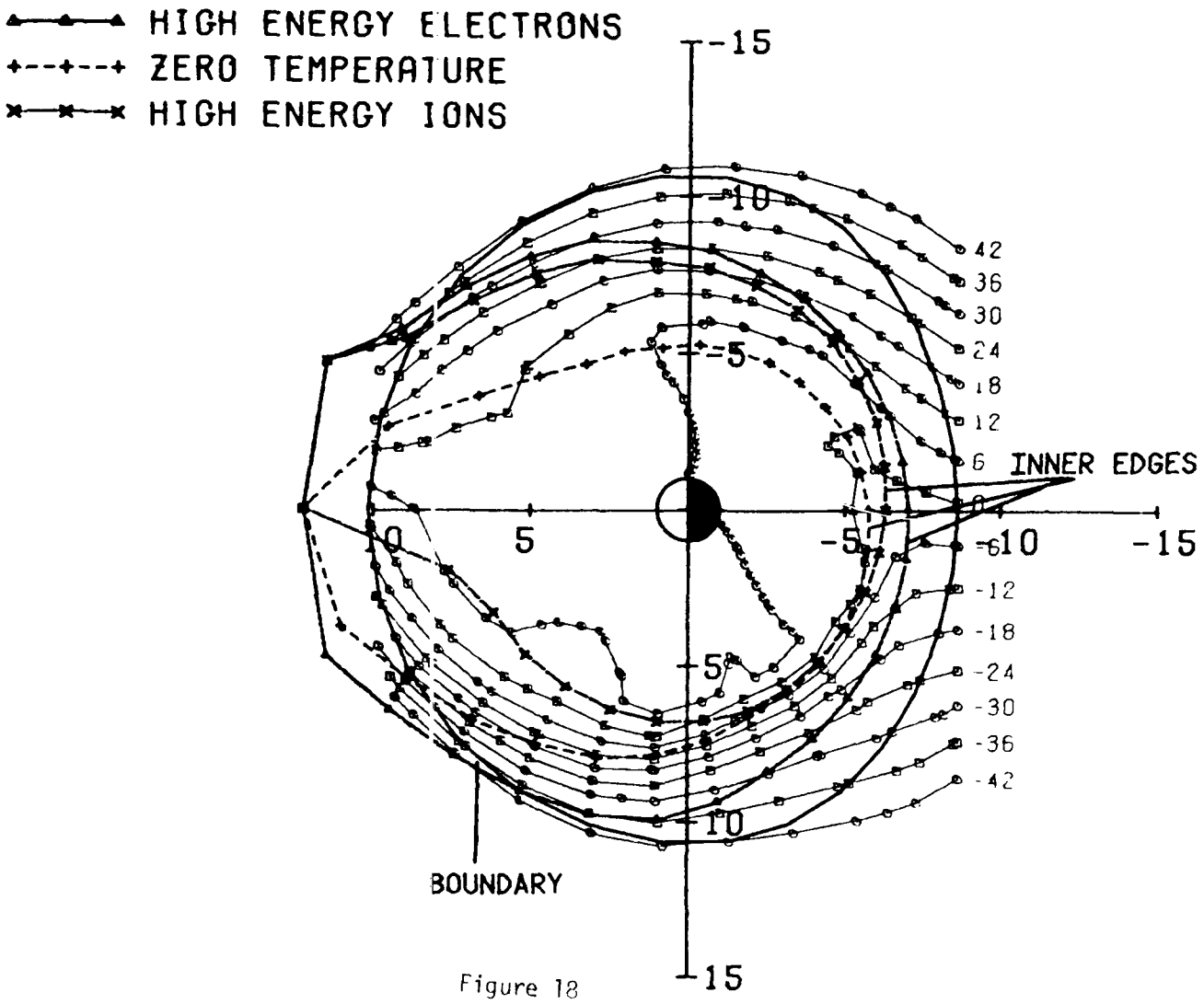

Figure 18

CASE 1 POTENTIAL CONTOURS W/O COROTATION (KV) K=2,11,21

TIME = 13:00

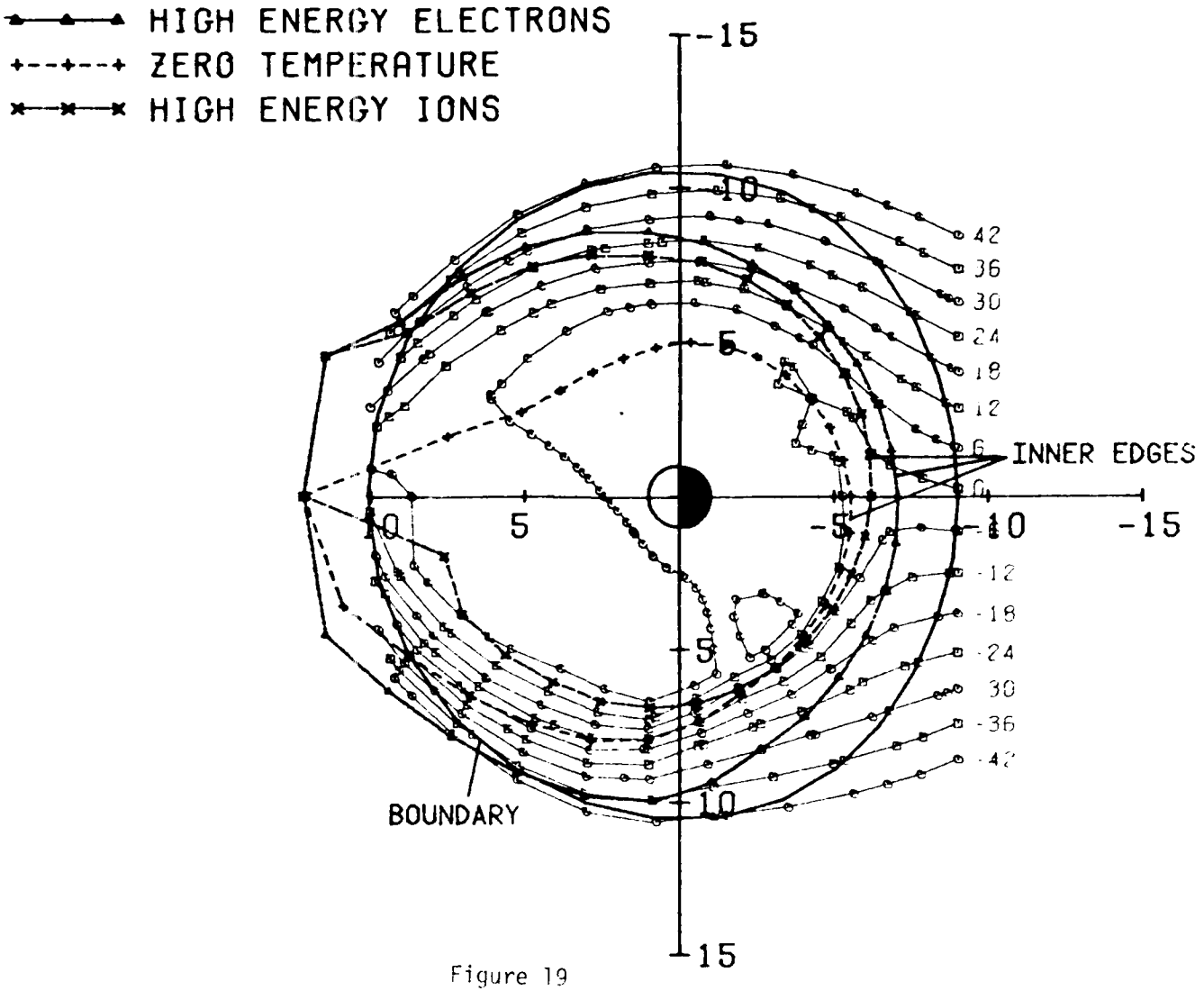

Figure 19

CASE 1 TOTAL ELECTRIC FIELD INCLUDING COROTATION

TIME = 13:00

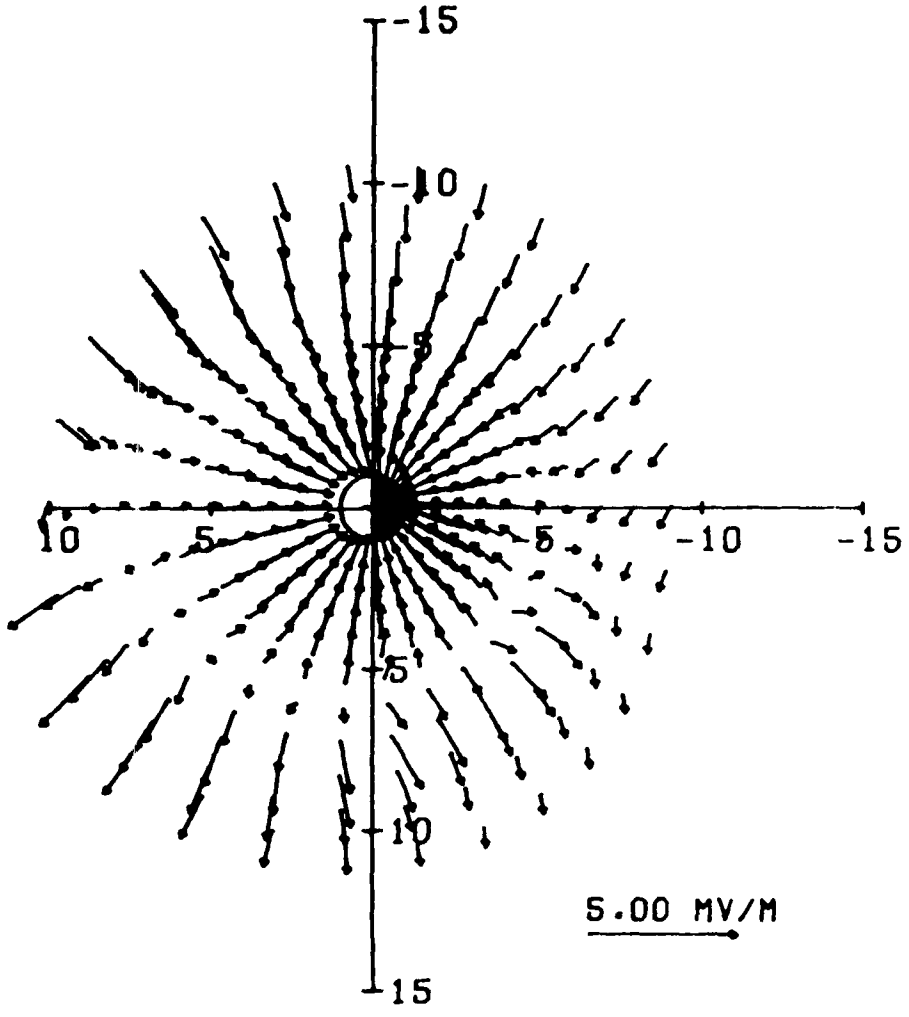

Figure 20

CASE 1 TOTAL VELOCITY FLOW FIELD IN EQUATORIAL PLANE

TIME = 13:00

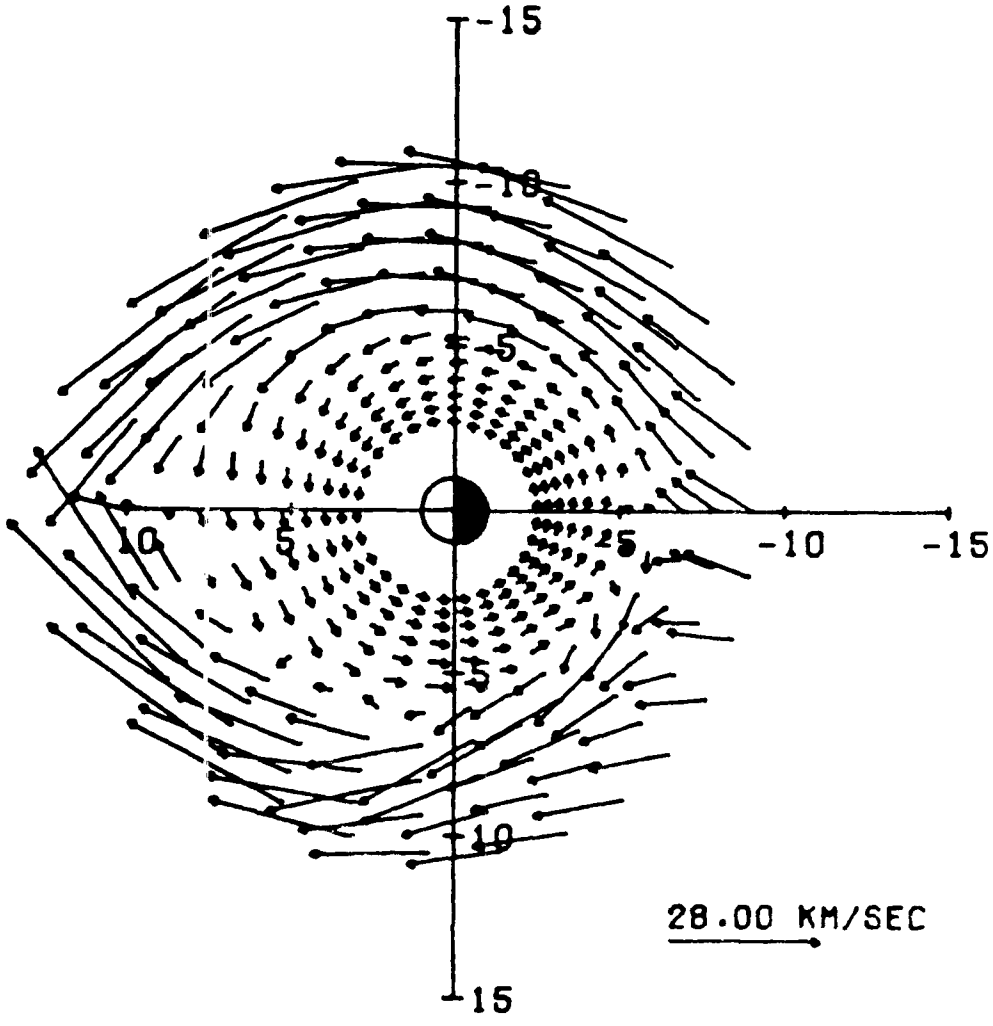

Figure 21

CASE 1 TOTAL VELOCITY FLOW FIELD IN IONOSPHERE IC=11

TIME = 13:00

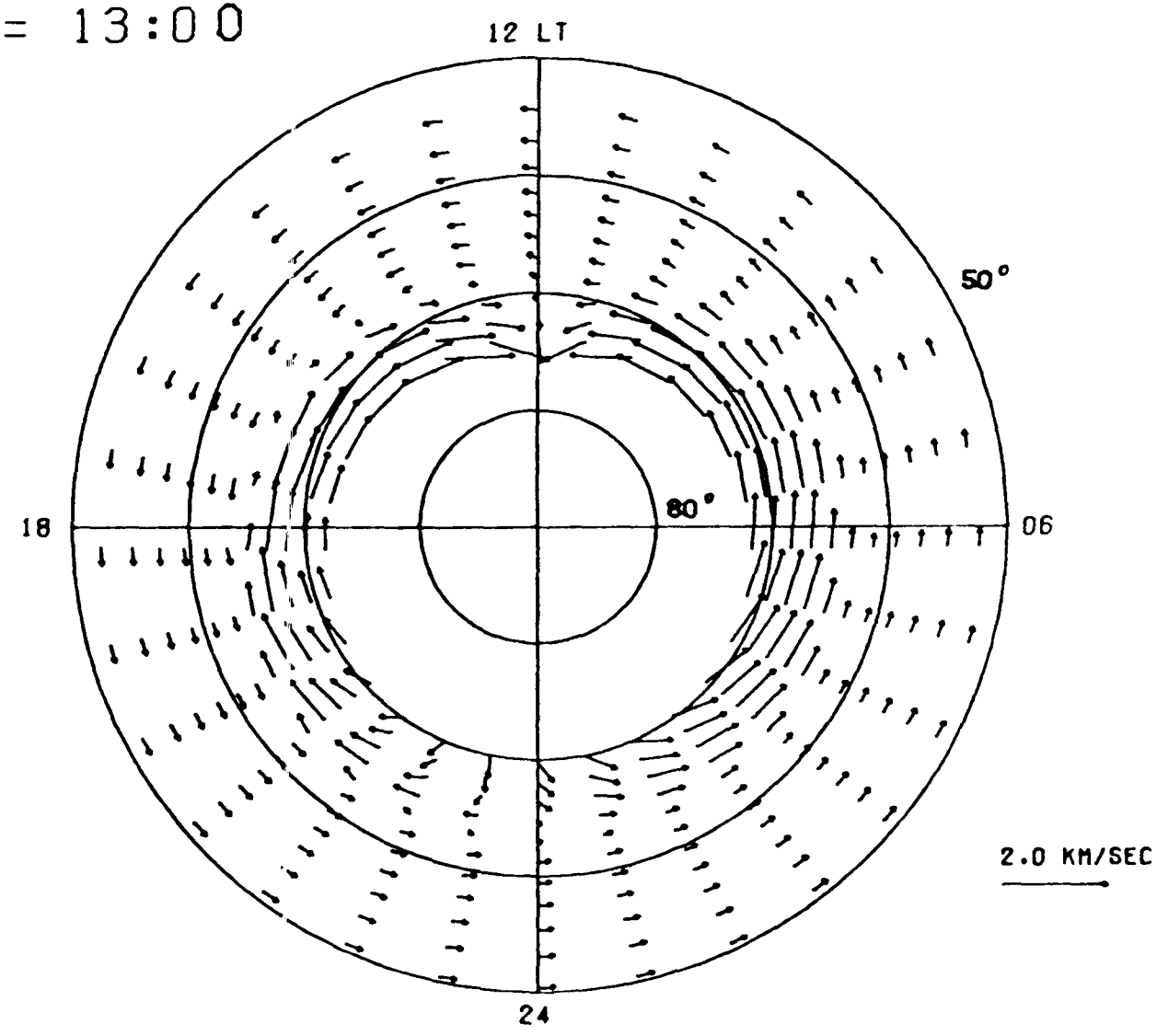

Figure 22

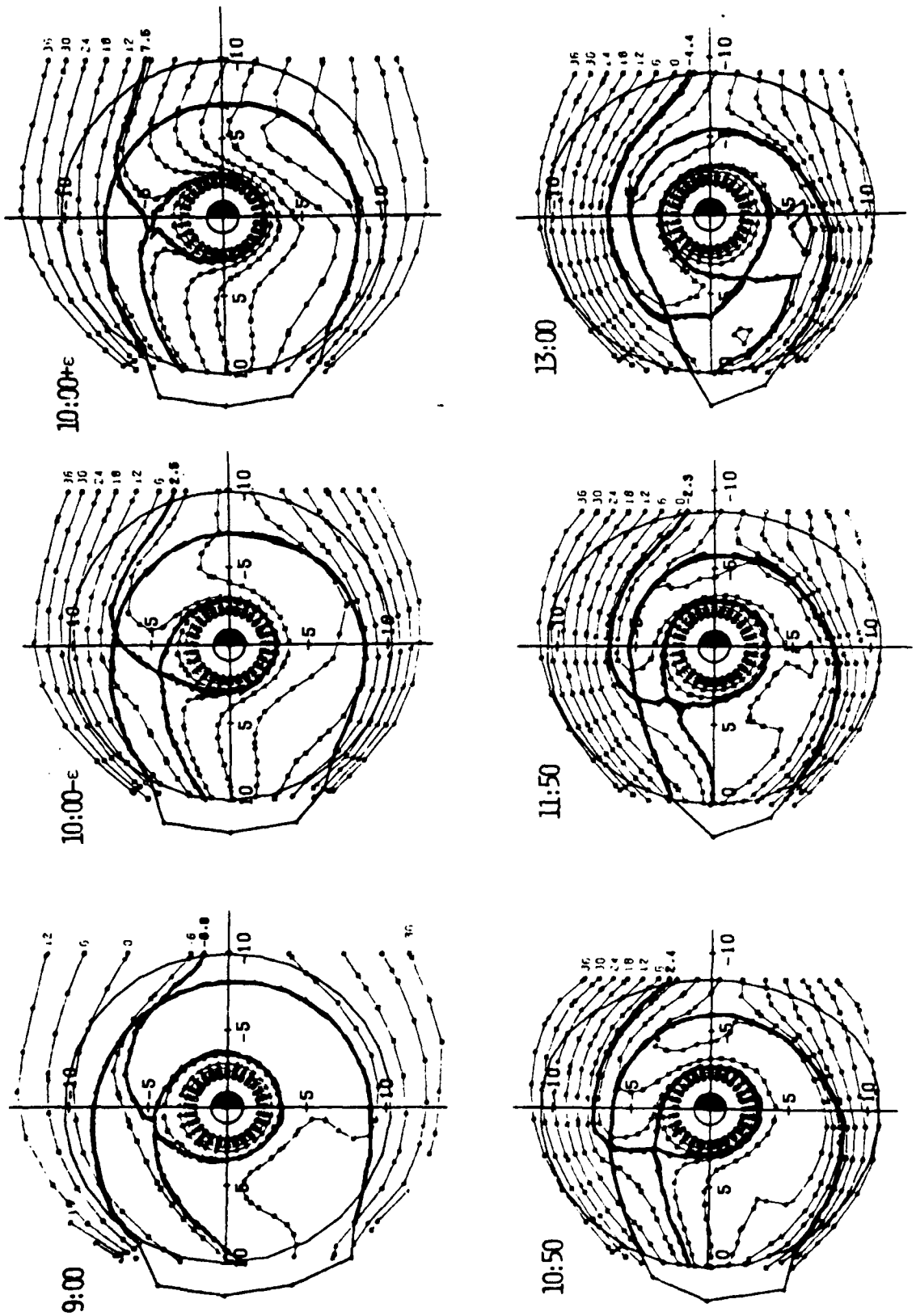

Figure 23

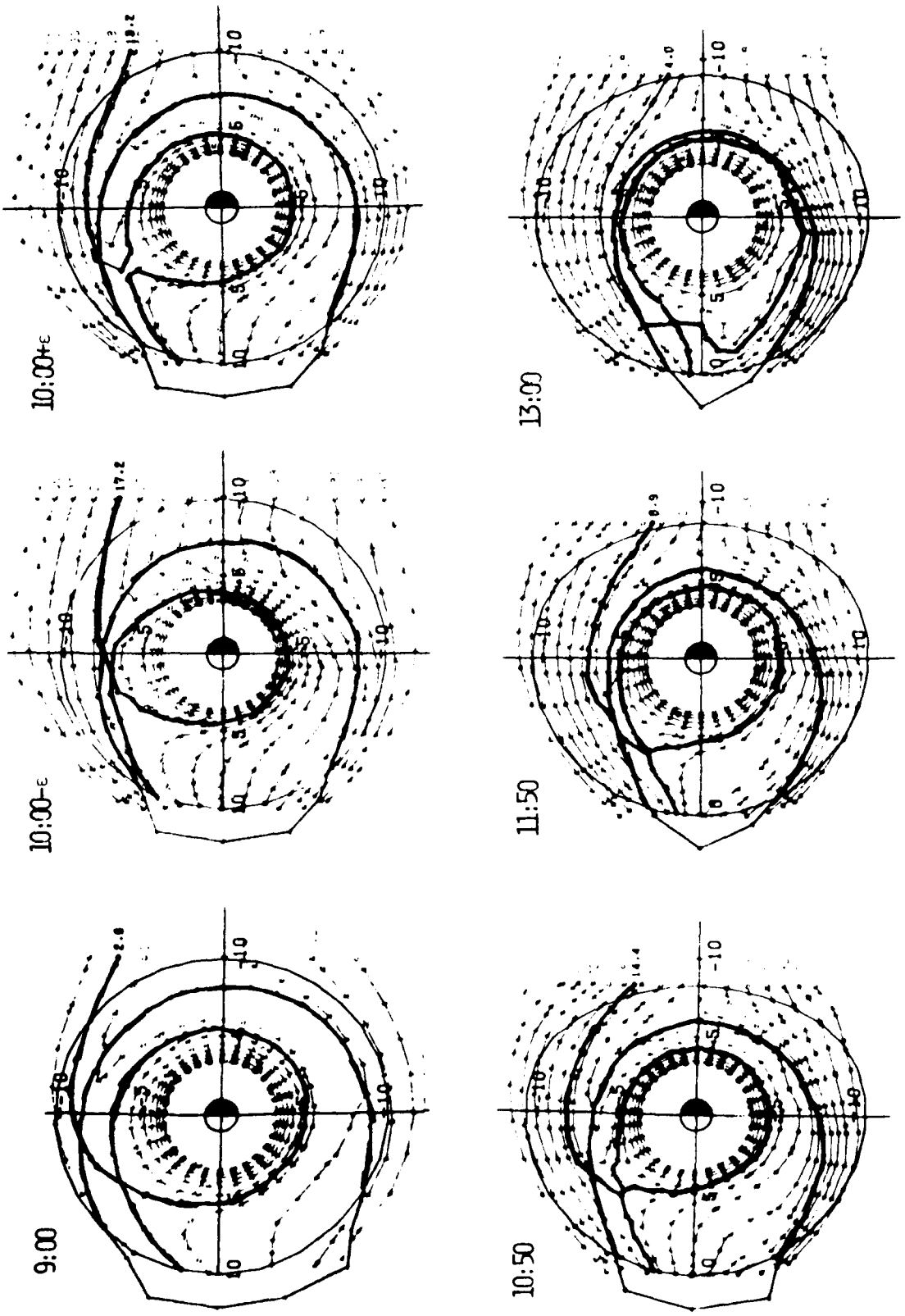

Figure 24

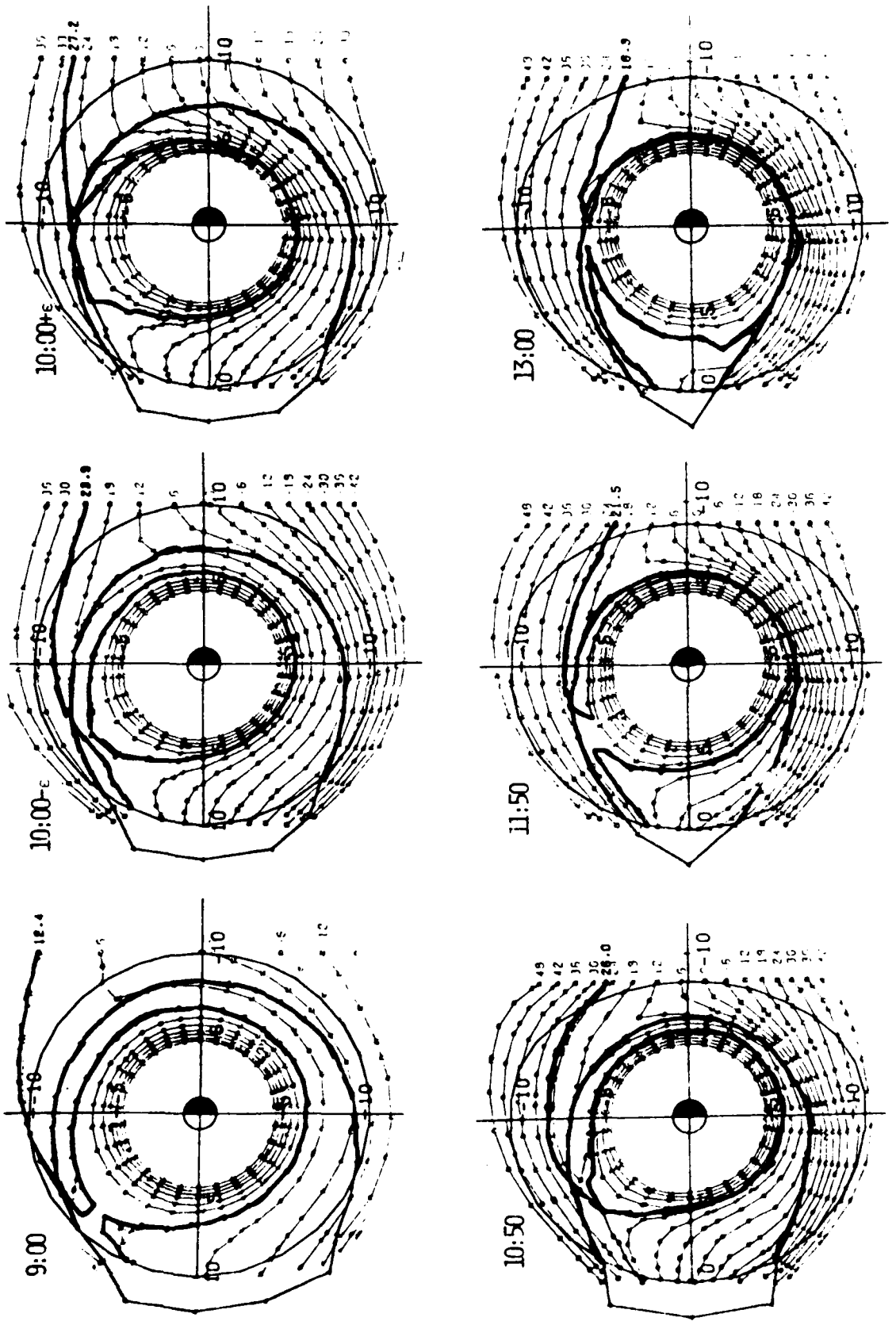

Figure 25

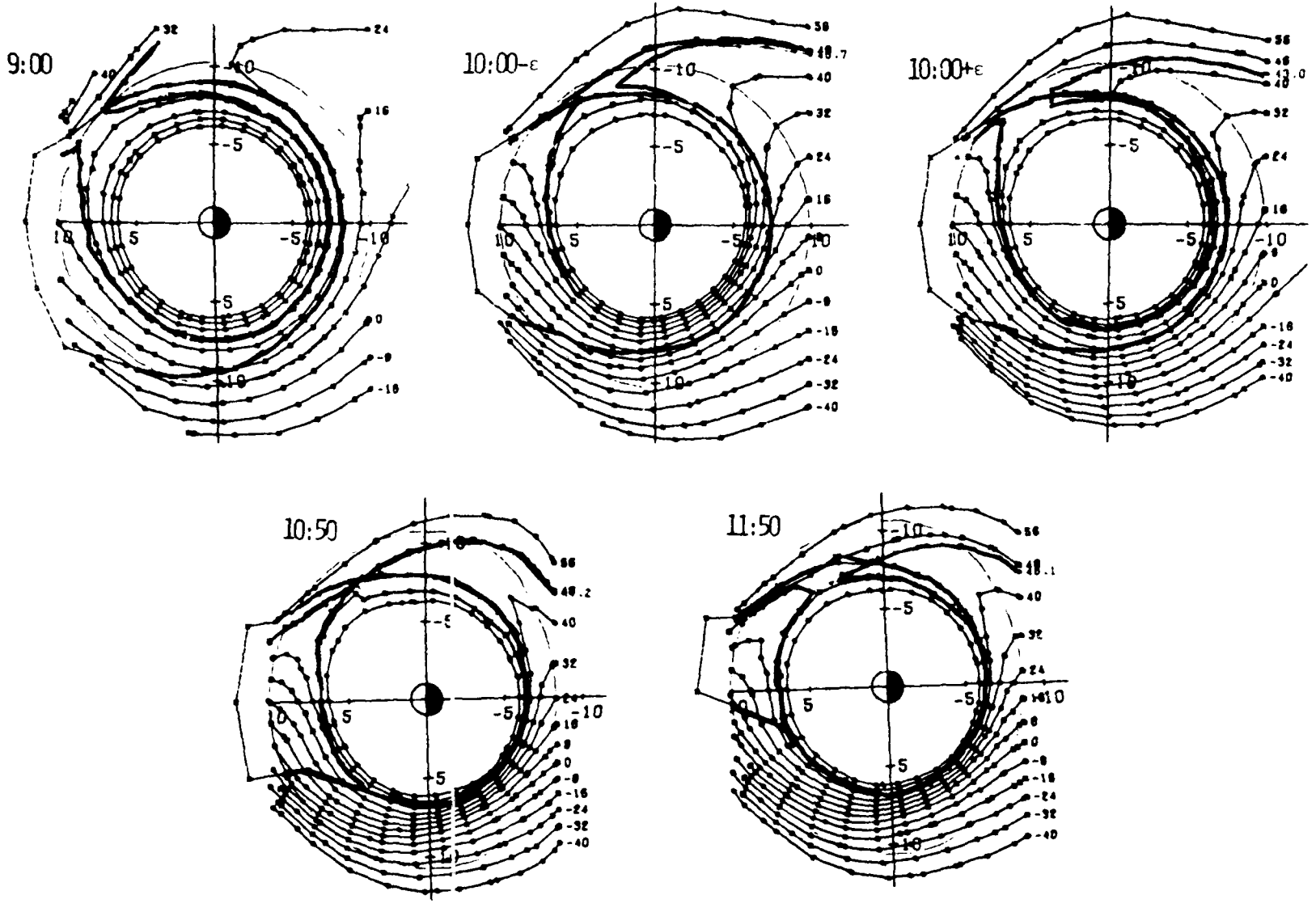

Figure 26


DATE
ILMED
-80